

A stable SPH model with large CFL numbers for multi-phase flows with large density ratios

Fang He^a, Huashan Zhang^{a,c}, Can Huang^{b,c,*}, Moubin Liu^{c,*}

^a Ocean College, Zhejiang University, Zhoushan, Zhejiang 316021, China

^b School of Mechanical and Materials Engineering, North China University of Technology, Beijing 100144, China

^c College of Engineering, Peking University, Beijing 100871, China

ARTICLE INFO

Article history:

Received 2 March 2021

Received in revised form 28 December 2021

Accepted 3 January 2022

Available online 7 January 2022

Keywords:

Multi-phase flows

Multi-phase interface

Smoothed particle hydrodynamics (SPH)

Shepard kernel

Large CFL numbers

ABSTRACT

The discontinuity across interface of multi-phase flows with large density ratios usually poses great challenges for numerical simulations. The smoothed particle hydrodynamics (SPH) is a meshless method with inherent advantages in dealing with multi-phase flows without the necessity of tracking the moving interfaces. In this paper, we develop a new weakly-compressible SPH model for multi-phase flows with large density ratios while allowing large CFL numbers. In the present SPH model, the continuity equation is first modified by eliminating the influence from particles of different phases based on the simple fact that different phases will not contribute when calculating the density for immiscible multi-phase flows; thus, the modified continuity equation will only consider the influence from neighboring particles of the same phase. The pressure and density of the particles of other phases are then re-initialized by using the Shepard interpolation function. The present multi-phase SPH model has been tested by four numerical examples, including the two-phase hydrostatic water, standing waves, liquid sloshing, and dam breaking. It has been demonstrated that the present multi-phase SPH model can obtain satisfactory results stably, even at large CFL numbers, and this means that large time steps can be employed. Therefore, the present multi-phase SPH model can significantly save computational cost through using large time steps, especially for large-scale problems with a large number of particles.

© 2022 Elsevier Inc. All rights reserved.

1. Introduction

Multi-phase flows consisting of two or more different fluids widely exist in nature and daily life. The computer modeling of multi-phase flows is more challenging than modeling single-phase flows due to the evolving interfaces with discontinuities in field properties (density, velocity, etc.) between different fluid phases. Generally, special algorithms such as the volume of fluid (VOF) method [1,2], the level set method [3–5], and the front tracking method [6], are usually necessary to track the multi-phase interface for the grid-based methods (i.e., finite volume method [7], finite difference method [8] and finite element method [9]). Compared to the grid-based methods, the smoothed particle hydrodynamics (SPH) is a particle and meshless method in the Lagrangian frame. It has been widely applied in various fields, including multi-phase flows [10,11], free-surface flows [12,13], plastic flow problems [14–16], fluid-structure interactions [17–21], and complex

* Corresponding authors.

E-mail addresses: huangcancan@ncut.edu.cn (C. Huang), mbliu@pku.edu.cn (M. Liu).

flows with porous media [22,23]. Besides, many advanced algorithms, e.g., stable regularized moving least-squares (SRMLS) method [24] and particle refinement scheme [25], have also been developed to overcome the low accuracy caused by the irregular particle distribution and the truncation of kernel function support domain. Nowadays, SPH has been proven to be a powerful method without tracking the moving interfaces [26,27]. In fact, the elementary volume of the fluid follows its Lagrangian motion in SPH simulations so that the evolving interface can be described clearly, and this is essentially beneficial to solve multi-phase flow problems.

The main challenge of SPH simulations for multi-phase flows is closely related to the discontinuity across the interface of multi-phase flows, especially when with large density ratios. Colagrossi and Landrini [28] derived a multi-phase SPH model that can effectively deal with the discontinuity in two-dimensional interface flows. They used the moving-least-square interpolation to re-initialize the density frequently, which removes the small-scale pressure oscillations. Besides, the discrete gradient based on volume is adopted to compensate for the density discontinuity at the interface. Finally, the air-water flow with interface breaking and air-entrapment can be easily treated, and stable results can be obtained. Hammani et al. [29] introduced a diffusive term into the multi-phase SPH model originally proposed by Grenier et al. [30] to remove numerical noise, and then improve the estimation of the particles spatial distribution and the pressure field. Some methods have been developed to overcome the instabilities caused by the multi-phase interface, such as the surface tension model [31], pairwise force model [32], and summation density approach [33]. For example, Adami et al. [31] proposed a new surface tension model to ensure the accuracy and stability of the multi-phase interface, and successfully applied the model to the three-dimensional multi-phase interface. Chen et al. [34] converted the density of heterogeneous particles into the same phase based on the continuity assumption of the interface pressure, and set a threshold value for density to avoid negative pressure and numerical divergence. They successfully developed a multi-phase SPH model suitable for complex interfaces and large density ratios. Rezavand et al. [35] added a repulsive force model for the multi-phase interface to avoid particles of different phases blended with each other, thus the stability of the interface can be well maintained. In addition, a projection-based particle method was proposed by Khayyer et al. [36] for simulating the discontinuous density field at the multi-phase interface and the multi-phase flow with large density ratios. They coupled the multi-fluid continuous system with the Optimized Particle Shifting (OPS) technique to keep the regularity of particles at the free surface and multi-phase interface.

As for the multi-phase incompressible SPH, Hu et al. [37] proposed a multi-phase incompressible SPH (ISPH) model where zero-density-variation condition and velocity-divergence-free condition are introduced by a fractional time-step method. Meanwhile, they proposed a novel multi-phase projection method to maintain the obvious density and viscosity discontinuity, in which the differentiable viscosity or density is not required for the discrete gradient and divergence operators. In addition, this multi-phase ISPH model is further developed with a constant-density approach in [38] for flows with large density ratios. Shao [39] presented two multi-phase ISPH models, i.e., coupled and decoupled ISPH models, to simulate multi-phase flows. The coupled ISPH model ignores the discontinuity of the multi-phase interface and directly adopts the standard ISPH method across the interface, while the decoupled ISPH model takes different phases into consideration separately and applies the continuity of pressure and shear stress to treat the multi-phase interface. The decoupled ISPH shows a better agreement with relevant data due to the careful and accurate treatment of the multi-phase interface. Lind et al. [40] applied ISPH to model the water phase and compressible SPH to model the air phase, therefore two-phase flows with large density ratio can be effectively simulated. Nair and Tomar [41] also proposed a compressible-incompressible SPH model to simulate a gas-liquid system where the gas is assumed to be a compressible fluid and the liquid is considered as an incompressible fluid. A penalty approach is applied in the solution for the pressure Poisson equation and the gradient approximation of the pressure to set the Dirichlet boundary condition at the free surface. Yang et al. [42] treated both phases in two-phase flows as weakly compressible fluids and presented a comprehensive multi-phase SPH model with damping technique and interfacial force. The boundary force is introduced to the boundary model for preventing particle penetration. Many tests with large density ratios (up to 1000) demonstrate the robustness and correctness of the comprehensive multi-phase SPH model. In the context of strongly compressible multi-phase flows, the physical sound speed of the gas has been adopted by Sun et al. [43] in the equation of state for the actual fluid compressibility, whereas the artificial sound speed is used in the time step calculation and diffusive terms to maintain the numerical stability. Meanwhile, the appropriate neighboring particles are maintained by adjusting smoothing particle lengths. The particle volume variation may be out of control especially around the multi-phase interface between different compressibility, therefore a novel adaptive scheme is presented to deal with the over-expanded or over-compressed problems.

Recently, the Riemann solver has been widely utilized in multi-phase flow simulations. Rezavand et al. [44] applied a low-dissipation Riemann solver to stabilize the interface interaction and added a transport-velocity formulation into the phase with lower density to alleviate non-physical voids. Meng et al. [45] proposed a multi-phase SPH model for simulating the complex interfacial flows based on Roe's approximate Riemann solver with a dissipation limiter. Meanwhile, they considered the effect of the realistic compressibility on the lighter fluid, which leads to a larger time step. The computational cost is reduced by an optimized adaptive linked-list search algorithm. To consider the effect of air on water entry problems, Yang et al. [46] described a novel two-phase model coupling with structure by using an improved Riemann solver. The Riemann dissipation is reduced by an intermediate pressure developed in the momentum equation. Besides, the instability of multi-phase interfaces caused by the strong impact is improved by a switch-function-based Riemann solver dissipation.

Suresh et al. [47] conducted a comparative study between the continuity density approach and the summation density approach in the SPH modeling of multi-phase flows. According to their results, the summation density approach is preferred

for the multi-phase flow with large density ratios due to its good stability and relatively large feasible time step, whereas the continuity density approach is more suitable for small density ratios. Up to now, to the best of the authors' knowledge, it is still a big challenge for the continuity density approach to simulate multi-phase flow with large density ratios. The associated CFL numbers are usually very small, which causes high computational costs. However, since the continuity density approach produces time-rate density variation closely relating to the compressibility and energy variation of the fluids, this approach is of great potential for the simulation of multi-phase flows in essence, especially those with large density ratios and extreme loadings (e.g., underwater explosion). In this study, to improve the efficiency and stability of the continuity density approach when simulating multi-phase flows with large density ratios, we develop a novel multi-phase SPH model with two modifications on the conventional multi-phase SPH method. The first modification is to eliminate the influence from the interacting particles of the other phase when approximating the continuity equation. The second is to re-initialize the pressure and density of the interacting particles of the other phase based on the Shepard kernel. It is noted that the first modification comes from the simple fact that for an immiscible multi-phase flow, one phase is not able to be converted to the other phase, and therefore, only particles of the same phase have contributions on approximating continuity equations.

The remaining parts of the paper are organized as follows. In Section 2, the governing equations, basic concepts of SPH method, and conventional multi-phase SPH model are briefly introduced. In Section 3, a novel multi-phase SPH model is developed, together with boundary treatment and time integration algorithm details. In Section 4, four benchmark cases, including the two-phase hydrostatic water, standing waves, liquid sloshing and dam breaking are provided to test the stability, efficiency, convergence and accuracy of the proposed multi-phase SPH model. The work ends in Section 5 with some concluding remarks.

2. SPH modeling of multi-phase flows with continuity density

2.1. Governing equations

In this work, the Euler equations are adopted as the governing equations for multi-phase inviscid flows. The continuity and momentum equations in the Lagrangian frame are as follows

$$\frac{D\rho}{Dt} = -\rho \nabla \cdot \mathbf{u} \quad (1)$$

$$\rho \frac{D\mathbf{u}}{Dt} = -\nabla p + \rho \mathbf{f} \quad (2)$$

where D/Dt is the Lagrangian or material derivative, t the time, p the pressure, ρ the density, \mathbf{u} the velocity field, \mathbf{f} the body force. Here, the body force is gravity. $\nabla \cdot$ and ∇ are the divergence and gradient operators, respectively.

To make the above equations close, the state equation that relates the pressure with the density is considered as

$$p = c_0^2 (\rho - \rho_0) + p_{bg} \quad (3)$$

where ρ_0 is the referenced density (1000 kg/m³ for water and 1 kg/m³ for air). The background pressure p_{bg} is adopted to avoid the negative pressure [34] and a 500 Pa is used in this study unless other statements. The weakly compressible assumption requires that the Mach number should be less than 0.10. Therefore, the sound speed c_0 should be at least one order of magnitude larger than the maximum velocity of the flow [48,49], i.e., $c_0 \geq 10 \max(U_{\max}, \sqrt{p_{\max}/\rho_{0,w}})$, where U_{\max} is the maximum expected velocity, p_{\max} is the maximum expected pressure and $\rho_{0,w}$ is the referenced density of water. It is noted that the sound speed c_0 is kept constant for different phases as in Refs. [34,44], which makes the larger time step acceptable and enhances the computational performance significantly.

2.2. Basic concepts of SPH

Smoothed particle hydrodynamics is a particle method with Lagrangian characteristics, which discretizes the field function by using a set of particles with physical properties such as density, velocity and pressure. Generally, the SPH method involves kernel approximation and particle approximation. In the first step, i.e., kernel approximation, the field function $f(\mathbf{x})$ and its spatial derivatives are discretized by using kernel function as

$$\langle f(\mathbf{x}) \rangle = \int_{\Omega} f(\mathbf{x}') W(\mathbf{x} - \mathbf{x}', h) d\mathbf{x}' \quad (4)$$

$$\langle \nabla \cdot f(\mathbf{x}) \rangle = - \int_{\Omega} f(\mathbf{x}') \cdot \nabla W(\mathbf{x} - \mathbf{x}', h) d\mathbf{x}' \quad (5)$$

where $\langle \rangle$ is the SPH approximation, \mathbf{x} the spatial coordinates, Ω the support domain, \mathbf{x}' the spatial coordinates of the interacting particle in the support domain. $W(\mathbf{x} - \mathbf{x}', h)$ and $\nabla W(\mathbf{x} - \mathbf{x}', h)$ are the kernel function and its spatial derivatives (with respect to \mathbf{x}') based on smoothing length h and the relative position $\mathbf{x} - \mathbf{x}'$, respectively. The kernel function

$W(\mathbf{x} - \mathbf{x}', h)$ has the Dirac delta function property. The Gaussian function [50] is adopted as the kernel function in this work.

In the second step, i.e., particle approximation, Eqs. (4) and (5) are discretized by summing the kernel weight of interacting particles as [25,26,51]

$$\langle f(\mathbf{x}_i) \rangle = \sum_{j=1}^N f(\mathbf{x}_j) W_{ij} V_j \quad (6)$$

$$\langle \nabla \cdot f(\mathbf{x}_i) \rangle = \sum_{j=1}^N f(\mathbf{x}_j) \cdot \nabla_i W_{ij} V_j \quad (7)$$

where

$$V_j = \frac{m_j}{\rho_j} \quad (8)$$

$$W_{ij} = W(\mathbf{x}_i - \mathbf{x}_j, h) \quad (9)$$

$$\nabla_i W_{ij} = -\nabla_j W_{ij} = \frac{\mathbf{x}_i - \mathbf{x}_j}{r_{ij}} \frac{\partial W_{ij}}{\partial r_{ij}} = \frac{\mathbf{x}_{ij}}{r_{ij}} \frac{\partial W_{ij}}{\partial r_{ij}} \quad (10)$$

where i is the i -th particle in the problem domain, and j is the j -th interacting particle in the support domain of the particle i . N indicates the total number of neighboring particles in the support domain of particle i , m_j the mass of particle j , ρ_j the density of particle j , V_j the volume of particle j , $r_{ij} = |\mathbf{x}_i - \mathbf{x}_j|$ the distance between particles i and j .

2.3. Conventional multi-phase SPH model

There are various multi-phase SPH models [10,35,38,43,45]. In this work, the conventional multi-phase SPH model refers to the conventional SPH discretization scheme with a diffusive term and a corrected density re-initialization treatment, previously developed by the authors' team.

Using Eq. (7), the governing equations are discretized as

$$\frac{D\rho_i}{Dt} = -\rho_i \sum_j^N \mathbf{u}_j \cdot \nabla_i W_{ij} \frac{m_j}{\rho_j} \quad (11)$$

$$\rho_i \frac{D\mathbf{u}_i}{Dt} = -\sum_j^N p_j \nabla_i W_{ij} \frac{m_j}{\rho_j} + \rho_i \mathbf{f}_i \quad (12)$$

The integration of the kernel function derivatives among the symmetric domain is zero due to its odd function characteristic. Therefore, we can obtain the following formulae

$$0 = \rho_i \sum_j^N \mathbf{u}_i \cdot \nabla_i W_{ij} \frac{m_j}{\rho_j} \quad (13)$$

$$\mathbf{0} = -\sum_j^N p_i \nabla_i W_{ij} \frac{m_j}{\rho_j} \quad (14)$$

Combining Eqs. (13) and (14), Eqs. (11) and (12) can be rewritten as

$$\frac{D\rho_i}{Dt} = -\rho_i \sum_j^N (\mathbf{u}_j - \mathbf{u}_i) \cdot \nabla_i W_{ij} \frac{m_j}{\rho_j} \quad (15)$$

$$\rho_i \frac{D\mathbf{u}_i}{Dt} = -\sum_j^N (p_i + p_j) \nabla_i W_{ij} \frac{m_j}{\rho_j} + \rho_i \mathbf{f}_i \quad (16)$$

To reduce the high-frequency oscillations of pressure and stabilize the pressure field [29,48], the δ -SPH model and the artificial viscous term are introduced into the continuity equation and the momentum equation, respectively as

$$\frac{D\rho_i}{Dt} = -\rho_i \sum_j^N (\mathbf{u}_j - \mathbf{u}_i) \cdot \nabla_i W_{ij} \frac{m_j}{\rho_j} + \delta h c_0 \sum_j^N \psi'_{ij} \cdot \nabla_i W_{ij} \frac{m_j}{\rho_j} \quad (17)$$

$$\rho_i \frac{D\mathbf{u}_i}{Dt} = - \sum_j^N (p_i + p_j) \nabla_i W_{ij} \frac{m_j}{\rho_j} + \rho_i \mathbf{f}_i + \alpha_{ij,i} h c_0 \rho_{0,i} \sum_j^N \pi_{ij} \nabla_i W_{ij} \frac{m_j}{\rho_j} \quad (18)$$

where

$$\psi'_{ij} = 2 (\rho'_j - \rho_i) \frac{\mathbf{x}_j - \mathbf{x}_i}{|\mathbf{x}_{ij}|^2} \quad (19)$$

$$\rho'_j = \frac{p_j - p_{background}}{c_0^2} + \rho_{0,i} \quad (20)$$

$$\alpha_{ij,i} = \frac{2(\dim+2)\mu_{ij,i}}{\rho_{0,i}hc} = \frac{2(\dim+2)}{\rho_{0,i}hc} \frac{2\mu_i\mu_j}{\mu_i + \mu_j} \quad (21)$$

$$\pi_{ij} = \frac{(\mathbf{u}_j - \mathbf{u}_i) \cdot \mathbf{x}_{ji}}{|\mathbf{x}_{ij}|^2} \quad (22)$$

where $\rho_{0,i}$ is the referenced density of particle i , \dim is the spatial dimension. It is noted that the calculation of the diffusive term in the conventional multi-phase SPH model takes the particle of the other phase in the support domain into consideration. Therefore, the corrected density re-initialization treatment [34] is applied to get the equivalent density ρ'_j , i.e., Eq. (20), preventing the instability caused by the large density ratio. The coefficient δ determines the magnitude of the artificial diffusive term, and $\delta = 0.10$ is suggested for balancing the accuracy and stability [52]. $\alpha_{ij,i}$ is the combined artificial viscosity between the particles i and j if they are not of the same phase [7]. The artificial viscosity of water is $\alpha_w = 0.05$ unless other statements and the ratio of the dynamic viscosity between water and gas is $\mu_w : \mu_g = 40 : 1$. It is noted that the consistency of Euler equations recovers because of the vanishing of diffusion and viscous terms with the increase of the spatial resolution.

3. A novel multi-phase SPH model

The continuity equation represents the principle of mass conservation, and the mass of different phases should rigorously keep constant in immiscible multi-phase flows. It is noted that the SPH approximations of a function and its derivatives on a specific particle i are actually the averaged summation of the field functions over all neighboring particles (j from 1 to N) (see Eqs. (6) and (7)). In modeling multi-phase flows, the neighboring particles j interacting with a specific particle i may come from both the same phase or different phases with the particle i . To the best of the authors' knowledge, most of the existing research works consider the influence of particle j on the density change rate of particle i when calculating the continuity equation, no matter what kind of phase the particle j belongs to. We think that particles from different phases should not have any contribution when approximating the density of a particle from a specific phase, based on the fact that the multi-phase flow is immiscible while different phases are associated with time-constant mass. In other words, only particles from the same phase should be used in the approximation of continuity equation, while considering contributions from other phases are redundant and can cause non-conservative mass.

Meanwhile, we corrected the pressure and density when the phase of the interacting particle is different from the concerned particle. Hence, the continuity and momentum equations, i.e., (17) and (18), can be rewritten as

$$\frac{D\rho_i}{Dt} = -\rho_i \sum_{j \in \chi_i} (\mathbf{u}_j - \mathbf{u}_i) \cdot \nabla_i W_{ij} \frac{m_j}{\rho_j} + \delta h c_0 \sum_{j \in \Omega_i} \psi_{ij}^* \cdot \nabla_i W_{ij} \frac{m_j}{\rho_j} \quad (23)$$

$$\rho_i \frac{D\mathbf{u}_i}{Dt} = - \sum_{j \in \Omega_i} (p_i + p_j^*) \nabla_i W_{ij} \frac{m_j}{\rho_j} + \rho_i \mathbf{f}_i + \alpha_{ij,i} h c_0 \rho_{0,i} \sum_{j \in \Omega_i} \pi_{ij} \nabla_i W_{ij} \frac{m_j}{\rho_j} \quad (24)$$

where

$$\psi_{ij}^* = 2 (\rho_j^* - \rho_i) \frac{\mathbf{x}_j - \mathbf{x}_i}{|\mathbf{x}_{ij}|^2} \quad (25)$$

$$p_j^* = \begin{cases} \sum_{j' \in \Omega_i} p_{j'} W_{jj'}^S \frac{m_{j'}}{\rho_{j'}}, & j \notin \chi_i \\ p_j, & j \in \chi_i \end{cases}; \quad W_{jj'}^S = \frac{W_{jj'}}{\sum_{j' \in \Omega_j} W_{jj'} \frac{m_{j'}}{\rho_{j'}}} \quad (26)$$

$$\rho_j^* = \frac{p_j^* - p_{background}}{c_0^2} + \rho_{0,i} \quad (27)$$

where χ represents the particle of the same phase with the concerned particle in the support domain of the concerned particle, as shown in Fig. 1(a). Ω represents all kinds of particles in the support domain of the concerned particle, as shown in Fig. 1(b). p_j^* and ρ_j^* are the corrected pressure and density, respectively, where $W_{jj'}^S$ is known as the Shepard kernel [30]. j' is the particle in the support domain of particle j .

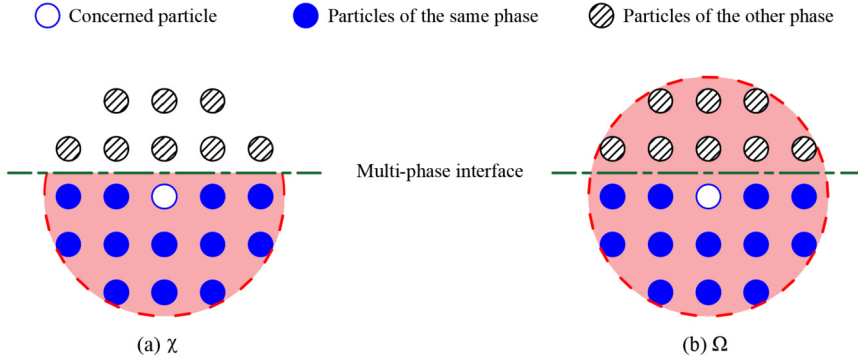


Fig. 1. Schematic illustration of interacting particles.

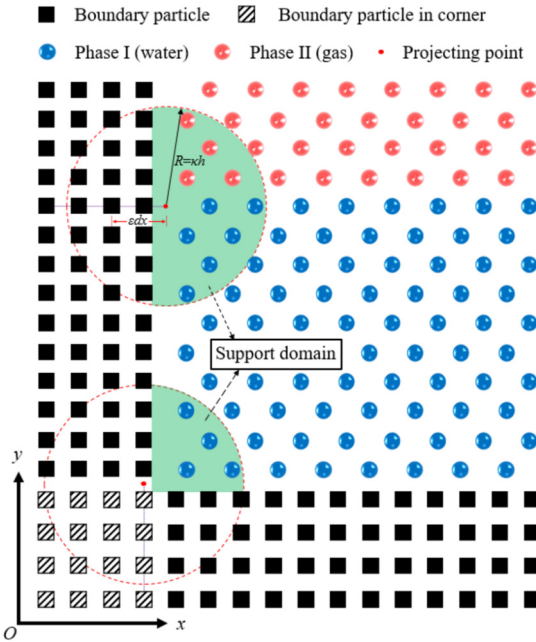


Fig. 2. Sketch of the projecting point, where R is the radius of support domain, h the smoothing length, dx the initial particle spacing, $\kappa = 3$ the coefficient of the support domain for Gaussian kernel, ε the coefficient of the projecting point. (For interpretation of the colors in the figure, the reader is referred to the web version of this article.)

3.1. Threshold value of density

The negative pressure is generally regarded as a factor leading to the numerical instability in the numerical simulation of fluid flows, which is more serious in multi-phase flows than single-phase flows. To avoid the negative pressure, we set a threshold value [34] of the density based on the background pressure as

$$\rho_i = -\frac{p_{bg}}{c_0^2} + \rho_{0,i}, \quad \text{if } p_i < 0 \quad (28)$$

When the pressure of the concerned particle p_i becomes minus, Eq. (28) is activated in all simulations so that the negative pressure can be significantly alleviated and even eliminated. Besides, Eq. (28) also ensures that all particles are weakly compressible and not expandable.

3.2. Boundary conditions for multi-phase flows

The wall particles and the ghost particles are created on the boundary. For the convenience of description, both the wall particles and ghost particles are called as boundary particles in this paper. The projecting points [53] with water or gas properties are used to update the physical properties of boundary particles for water or gas. Fig. 2 shows the relation between the projecting point and the boundary particle. The spatial coordinate of the projecting point is

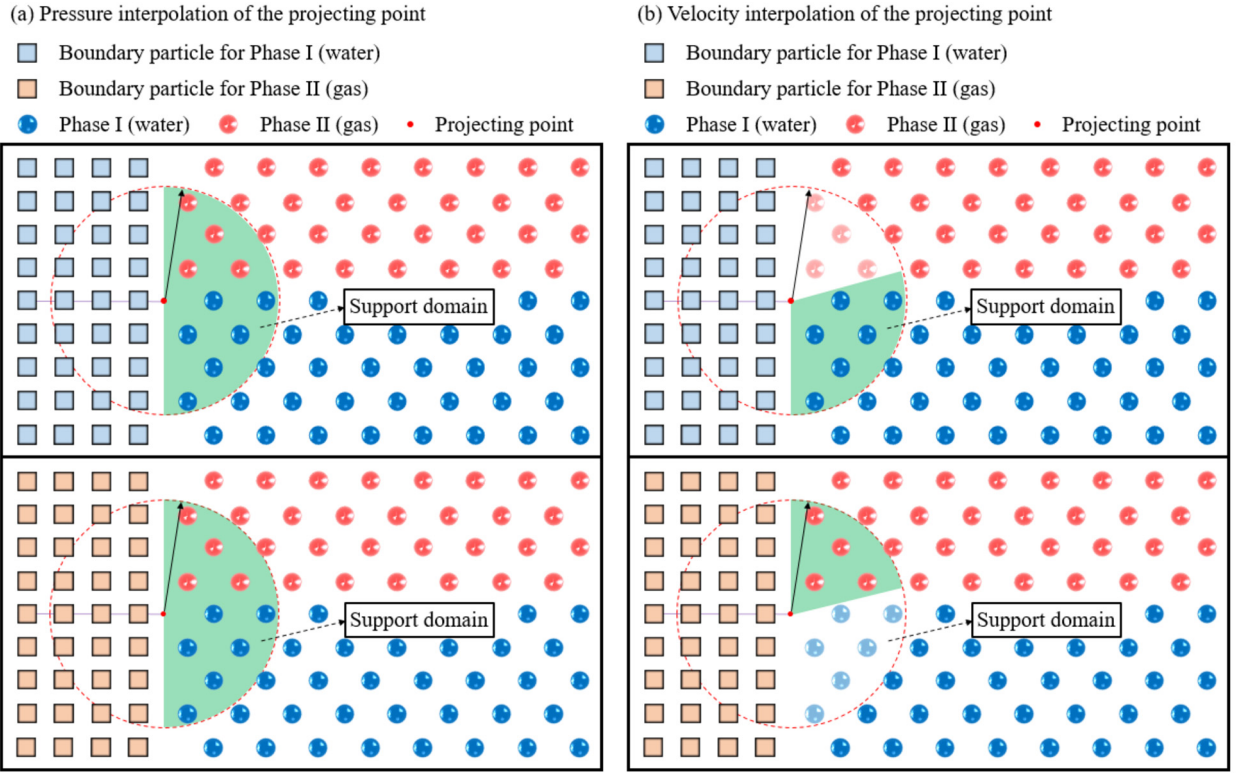


Fig. 3. Interpolation of the projecting point for different phases of the boundary particles: (a) pressure; (b) velocity. (For interpretation of the colors in the figure(s), the reader is referred to the web version of this article.)

$$\mathbf{x}_p = \mathbf{x}_b + \varepsilon d\mathbf{x}\mathbf{n}_b \quad (29)$$

where \mathbf{n}_b presents the unit normal vector of boundary toward the fluid domain. \mathbf{x}_b and \mathbf{x}_p indicate the coordinates of the boundary particle and the projecting point in space, respectively. There are four layers of the boundary particles, therefore, the coefficient ε is not constant. $\varepsilon = 0.5, 1.5, 2.5, 3.5$ is adopted for water and $\varepsilon = 1.0, 2.0, 3.0, 4.0$ for gas.

The pressure of the projecting point is calculated by summing the contribution of all fluid particles within the support domain (as shown in Fig. 3(a)) according to the continuity requirement of pressure. In contrast, the velocity of the projecting point is calculated by summing the contribution of the fluid particles belonging to the same phase of the projecting point (as shown in Fig. 3(b)) as follows

$$p_p = \frac{\sum_{f \in \Omega_p} p_f W_{pf} V_0}{\sum_{f \in \Omega_p} W_{pf} V_0} \quad (30)$$

$$\mathbf{u}_p = \frac{\sum_{f \in \chi_p} \mathbf{u}_f W_{pf} V_0}{\sum_{f \in \chi_p} W_{pf} V_0} \quad (31)$$

where p_p (\mathbf{u}_p) is the pressure (velocity) of the projecting point, p_f (\mathbf{u}_f) the pressure (velocity) of the fluid particle in the support domain of the projecting point. V_0 is the initial volume of fluid particles and keeps constant, which means that the fluid particles' contribution to the boundary particles is not affected by the volume of fluid particles. In Fig. 3(b), when the boundary particles are considered in calculating the water (gas) particles, only the water (gas) particles in the support domain of the projecting point are used to calculate the velocity of the projecting point.

After obtaining the pressure and velocity of the projecting point, the pressure and velocity of the boundary particle are updated based on p_p and \mathbf{u}_p , as

$$p_b = p_p - \rho_{0,b} \mathbf{a} \cdot (\varepsilon d\mathbf{x}\mathbf{n}_b) \quad (32)$$

$$\mathbf{u}_b^n = -\mathbf{u}_p^n \quad (33)$$

$$\mathbf{u}_b^\tau = \begin{cases} \mathbf{u}_p^\tau, & \text{slip} \\ \mathbf{0}, & \text{nonslip} \end{cases} \quad (34)$$

where p_b is the pressure of the boundary particle, \mathbf{a} the acceleration field, \mathbf{u}_b^n and \mathbf{u}_b^τ the normal velocity and tangential velocity of the boundary particle, \mathbf{u}_p^n and \mathbf{u}_p^τ the normal velocity and tangential velocity of the projecting point. It is noted that the direction of the velocity of the boundary particle in the corner is always toward the fluid to avoid penetrating. Taking the boundary particle in the left bottom corner in Fig. 2 as an example, the velocity of the particle is always in the positive direction of the x and y axes as

$$u_b^x = |\mathbf{u}_b^n \cdot \mathbf{e}_x + \mathbf{u}_b^\tau \cdot \mathbf{e}_x| \quad (35)$$

$$u_b^y = |\mathbf{u}_b^n \cdot \mathbf{e}_y + \mathbf{u}_b^\tau \cdot \mathbf{e}_y| \quad (36)$$

where u_b^x and u_b^y are the x -direction and y -direction velocities of the boundary particle, and \mathbf{e}_x and \mathbf{e}_y are the x -direction and y -direction basis vectors of the xOy coordinate system.

To overcome the instability suffered from the large density ratio, the mass and density of the boundary particle are decided by the phase of the fluid particle i . Therefore, when the boundary particle b is used for approximating the information of fluid particle i , the mass and density of the boundary particle are

$$m_b = \rho_{0,i} V_{0,i} \quad (37)$$

$$\rho_b = \frac{p_b - p_{background}}{c_0^2} + \rho_{0,i} \quad (38)$$

where m_b and ρ_b are the mass and density of the boundary particle, respectively.

Since the gas particle can be squeezed out of the boundary more easily by the water particle in the violent hydrodynamic events, a repulsive force model is used to prevent the gas particle from penetrating the boundary. The boundary force model used in this work is as follows [53]

$$\mathbf{f}_{gb} = \begin{cases} -c_0 \frac{(\mathbf{u}_g - \mathbf{u}_b) \cdot \mathbf{n}_b W_{gb} h^{\dim} \mathbf{n}_b}{|\mathbf{r}_{gb} \cdot \mathbf{n}_b|}, & (\mathbf{u}_g - \mathbf{u}_b) \cdot \mathbf{n}_b < 0 \\ 0, & (\mathbf{u}_g - \mathbf{u}_b) \cdot \mathbf{n}_b \geq 0 \end{cases} \quad (39)$$

where \mathbf{f}_{gb} indicates the repulsive force of the boundary particle b acting on the gas particle g .

3.3. Time integration

The Predictor-Corrector algorithm and the improved Euler method are used in this study to integrate the equations over time.

The Predictor-Corrector algorithm can be divided into three steps. Superscripts 0, 1/2 and 1 denote current, intermediate and updated values, respectively. First step: Predict the density, velocity and spatial coordinates of 1/2-th time step as

$$\begin{cases} \rho_i^{1/2} = \rho_i^0 + \frac{\Delta t}{2} \left(\frac{d\rho_i^0}{dt} \right) \\ \mathbf{u}_i^{1/2} = \mathbf{u}_i^0 + \frac{\Delta t}{2} \left(\frac{d\mathbf{u}_i^0}{dt} \right) \\ \mathbf{x}_i^{1/2} = \mathbf{x}_i^0 + \frac{\Delta t}{2} \left(\frac{d\mathbf{x}_i^0}{dt} \right) \end{cases} \quad (40)$$

Second step: Correct the density, velocity and spatial coordinates of 1/2-th time step as

$$\begin{cases} \bar{\rho}_i^{1/2} = \rho_i^0 + \frac{\Delta t}{2} \left(\frac{d\rho_i^{1/2}}{dt} \right) \\ \bar{\mathbf{u}}_i^{1/2} = \mathbf{u}_i^0 + \frac{\Delta t}{2} \left(\frac{d\mathbf{u}_i^{1/2}}{dt} \right) \\ \bar{\mathbf{x}}_i^{1/2} = \mathbf{x}_i^0 + \frac{\Delta t}{2} \left(\frac{d\mathbf{x}_i^{1/2}}{dt} \right) \end{cases} \quad (41)$$

Third step: Calculate all fluid variables at the next time step, i.e., 1-th time, as

$$\begin{cases} \rho_i^1 = 2\bar{\rho}_i^{1/2} - \rho_i^0 \\ \mathbf{u}_i^1 = 2\bar{\mathbf{u}}_i^{1/2} - \mathbf{u}_i^0 \\ \mathbf{x}_i^1 = 2\bar{\mathbf{x}}_i^{1/2} - \mathbf{x}_i^0 \end{cases} \quad (42)$$

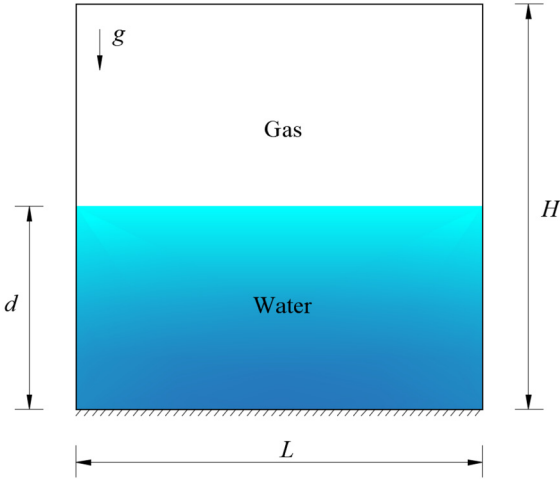


Fig. 4. Schematic diagram of two-phase hydrostatic water.

The improved Euler method can be divided into two steps, and its time-integration scheme is as follows

$$\begin{cases} \bar{\rho}_i^1 = \rho_i^0 + \Delta t \left(\frac{d\rho_i^0}{dt} \right) \\ \bar{\mathbf{u}}_i^1 = \mathbf{u}_i^0 + \Delta t \left(\frac{d\mathbf{u}_i^0}{dt} \right) \\ \bar{\mathbf{x}}_i^1 = \mathbf{x}_i^0 + \Delta t \left(\frac{d\mathbf{x}_i^0}{dt} \right) \end{cases} \quad (43)$$

$$\begin{cases} \rho_i^1 = \rho_i^0 + \frac{\Delta t}{2} \left(\frac{d\rho_i^0}{dt} + \frac{d\bar{\rho}_i^1}{dt} \right) \\ \mathbf{u}_i^1 = \mathbf{u}_i^0 + \frac{\Delta t}{2} \left(\frac{d\mathbf{u}_i^0}{dt} + \frac{d\bar{\mathbf{u}}_i^1}{dt} \right) \\ \mathbf{x}_i^1 = \mathbf{x}_i^0 + \frac{\Delta t}{2} \left(\frac{d\mathbf{x}_i^0}{dt} + \frac{d\bar{\mathbf{x}}_i^1}{dt} \right) \end{cases} \quad (44)$$

Note that the pressure is updated by the state equation, i.e., Eq. (3). The choice of time step Δt for both Predictor-Corrector algorithm and the improved Euler method is determined by the advection constraint $\Delta t \leq \text{CFL} \cdot h/c_0$ [54] for all simulations for the sake of simplicity.

4. Numerical result and discussion

In this section, the two-phase (water and gas) hydrostatic water and standing wave are tested to validate the stability, efficiency and convergence of the proposed multi-phase SPH model. Furthermore, the violent flows, i.e., the liquid sloshing and two-phase dam breaking, are used to validate the stability for the simulations of complex breaking interfaces.

4.1. Two-phase hydrostatic water

The two-phase hydrostatic water is divided into two parts of water and gas, as shown in Fig. 4. The length L and height H of the tank are both 1.0 m, and the initial water depth d is 0.5 m. The sound speed is adopted as $c_0 = 50.0$ m/s. We place water particles and gas particles on a Cartesian grid with an initial particle spacing $dx = d/50$, where the reference densities of water and gas are 1000 kg/m 3 and 1 kg/m 3 , respectively.

4.1.1. Stability analysis

Fig. 5 shows the zoom-in view of the multi-phase interface of the two-phase hydrostatic water simulated by the present multi-phase SPH model with the Predictor-Corrector algorithm. From Fig. 5 (d), it can be observed that the free surface of water predicted by the conventional multi-phase SPH model with $\text{CFL} = 0.20$ becomes unstable, where the water particles

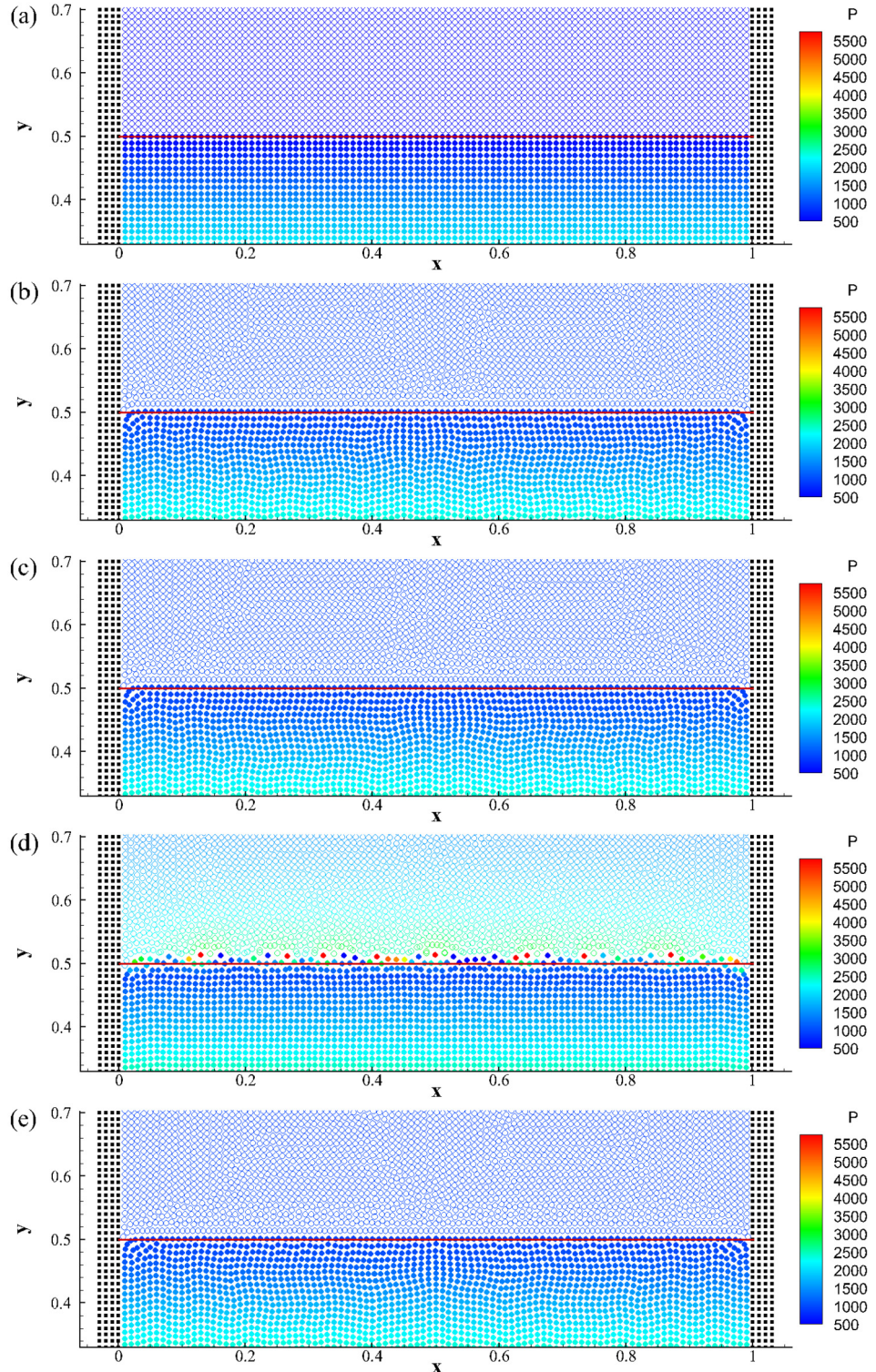


Fig. 5. Zoom-in view of interface of two-phase hydrostatic water by the present multi-phase SPH model with the Predictor-Corrector algorithm: (a) initial condition at $t(g/d)^{0.5} = 0$; (b) present multi-phase SPH model at $t(g/d)^{0.5} = 35.43$ and $\text{CFL} = 0.50$; (c) present multi-phase SPH model at $t(g/d)^{0.5} = 35.43$ and $\text{CFL} = 0.20$; (d) conventional SPH for multi-phase flows at $t(g/d)^{0.5} = 5.67$ and $\text{CFL} = 0.20$; (e) conventional SPH for multi-phase flows at $t(g/d)^{0.5} = 35.43$ and $\text{CFL} = 0.10$.

at the multi-phase interface fluctuate and the extreme pressure occurs leading to earlier termination of the simulation. It is noted that we only show the prediction by the conventional multi-phase SPH model with $CFL = 0.20$ at $t(g/d)^{0.5} = 5.67$ in Fig. 5 (d) due to its earlier termination. In contrast, the multi-phase interface at $t(g/d)^{0.5} = 35.43$ obtained by the present multi-phase SPH model is still stable and smooth no matter at $CFL = 0.20$ in Fig. 5 (c) or even at larger $CFL = 0.50$ in Fig. 5 (b). In addition, the free surface of the water and the pressure distribution predicted by the present multi-phase SPH model are consistent with the initial condition in Fig. 5 (a). When the CFL number decreases from 0.20 to 0.10, Fig. 5 (e) shows that the conventional multi-phase SPH model can obtain satisfactory results, and it can be concluded that the conventional multi-phase SPH model has the ability to maintain good stability and accuracy at the smaller CFL numbers. However, it does not help large-scale simulations due to the expensive computational costs.

Fig. 6 shows the zoom-in view of the multi-phase interface of the two-phase hydrostatic water simulated by the present multi-phase SPH model with the improved Euler method. Compared to Fig. 5, the simulations by the present multi-phase SPH model with the improved Euler method are similar to those by the Predictor-Corrector algorithm. The interfaces between the water and the gas predicted by the present multi-phase SPH model are consistent with the initial condition in Fig. 6(a) not only at $CFL = 0.20$ in Fig. 6(c), but also at $CFL = 0.50$ in Fig. 6(b). Though the conventional multi-phase SPH model could give a satisfactory result at $CFL = 0.10$ in Fig. 6(e), it still could not maintain the stable interface at $CFL = 0.20$ in Fig. 6(d) with the unsmoothed pressure field and early termination.

4.1.2. Energy conservation

The energy conservation of the present multi-phase SPH simulation is discussed according to the following dimensionless parameters

$$E^* = \frac{E}{E_0} \quad (45)$$

$$E_{k,f}^* = \frac{E_{k,f}}{E_0} \quad (46)$$

$$E_{p,f}^* = \frac{E_{p,f}}{E_0} \quad (47)$$

where E is the mechanical energy, E_0 the initial mechanical energy, E_k the kinematic energy, E_p the potential energy. The subscript f indicates the fluid phase (w for water and g for gas).

Fig. 7 shows the dissipation of total energy obtained by the present multi-phase SPH model with different time-integration schemes. It can be found that the dissipation curves of different CFL numbers almost coincide regardless of the improved Euler method or Predictor-Corrector algorithm, which manifests that the simulation of the two-phase hydrostatic water by the present multi-phase SPH model also converges at large CFL numbers (i.e., 0.50) in different time-integration schemes. Unless otherwise specified, the Predictor-Corrector algorithm is used as the integral format in the following discussions, since both integral formats would not make difference to the results by the present multi-phase SPH model.

Fig. 8 plots the evolution of kinematic energy for water and gas, respectively, in the two-phase hydrostatic water simulations. In terms of water in Fig. 8 (a), the early-stage oscillations happen. The second peak occurs both in the conventional and present SPH models. Subsequently, the kinematic energy of water tends to be a stable value close to zero, indicating that the two-phase simulations of hydrostatic water gradually become stable. On the other hand, it can be observed in Fig. 8 (b) that the kinematic energy of gas predicted by the conventional multi-phase SPH model with $CFL = 0.10$ tends to be zero after a period of oscillation. Differently, the kinematic energy of gas predicted by the present multi-phase SPH model with $CFL = 0.50$ steeply rises to a peak value and sharply declines to the zero level without the oscillation.

Fig. 9 plots the evolution of potential energy for water and gas, respectively, in the two-phase hydrostatic water simulations. The potential energy of water gradually dissipates, whereas the potential energy of gas initially skips and declines to a level without dissipation. The dissipation of the potential energy of water results in the main dissipation of the total energy because the potential energy of water makes up the vast majority of total energy. All numerical results have clearly shown that the present multi-phase SPH model with $CFL = 0.50$ can obtain results close to the conventional multi-phase SPH model with $CFL = 0.10$, which manifests that the present multi-phase SPH model has good characteristics of energy conservation even with a larger CFL number. Therefore, it can be demonstrated that the present multi-phase SPH model has advantages in terms of stability and computational cost compared to the conventional multi-phase SPH model.

4.2. Two-phase standing waves

The standing wave is a periodic transition between the kinematic energy and the potential energy. According to the linear theory, the standing wave would evolve without attenuating any wave amplitude due to the total conserved energy. Nevertheless, the SPH approximation here could not preserve the total conserved energy due to the artificial viscous term in the momentum equation. As a result, the kinematic energy tends to be zero and the standing wave is to be damped for a long time simulation. Antuono & Colagrossi [55] extended the analytical expression of the energy dissipation to the moderate Reynolds numbers to provide a benchmark for numerical solvers' validation. In this section, the standing waves

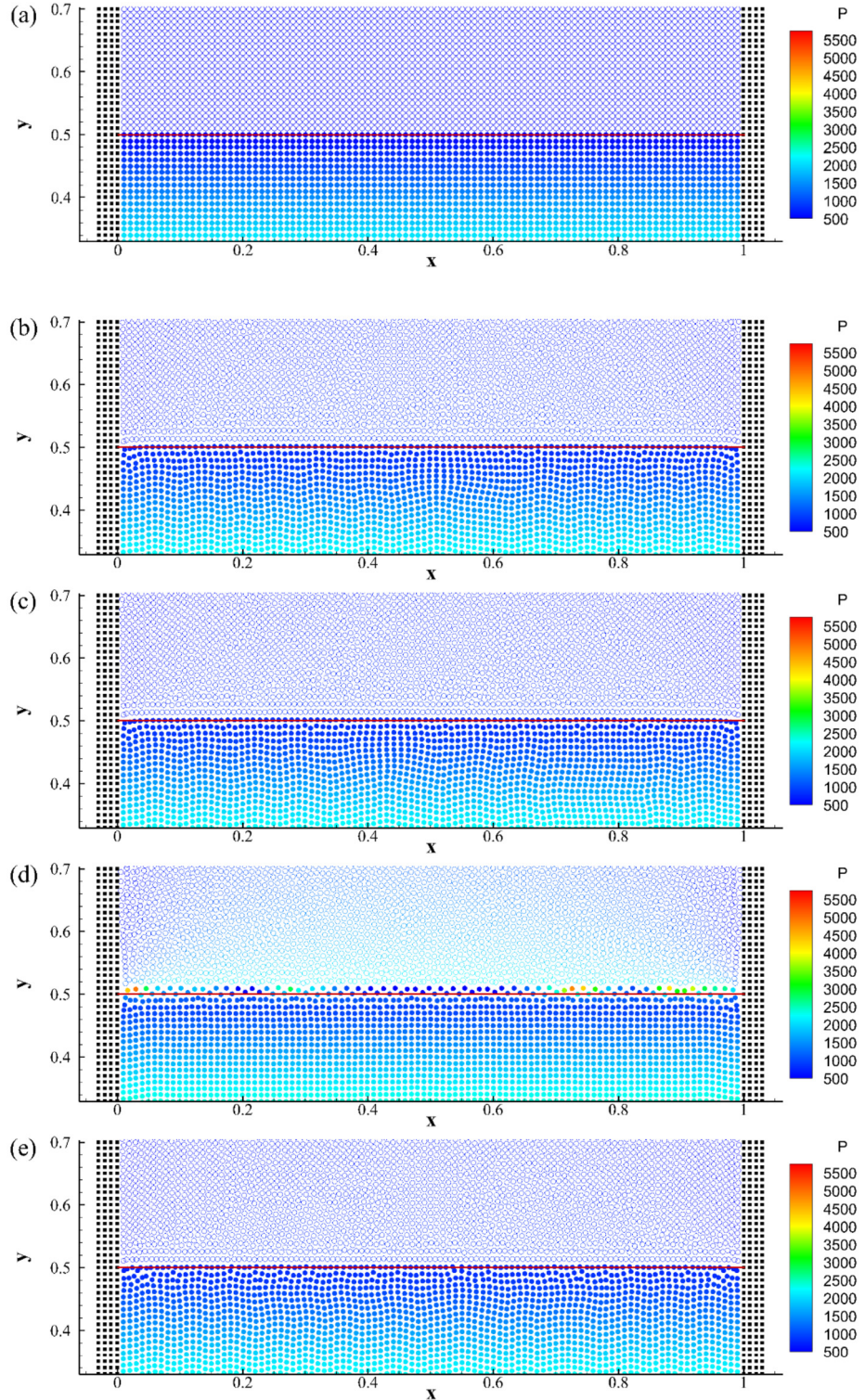


Fig. 6. Zoom-in view of interface of two-phase hydrostatic water by the present multi-phase SPH model with the improved Euler method: (a) initial condition at $t(g/d)^{0.5} = 0$; (b) present multi-phase SPH model at $t(g/d)^{0.5} = 35.43$ and CFL = 0.50; (c) present multi-phase SPH model at $t(g/d)^{0.5} = 35.43$ and CFL = 0.20; (d) conventional SPH for multi-phase flows at $t(g/d)^{0.5} = 8.33$ and CFL = 0.20; (e) conventional SPH for multi-phase flows at $t(g/d)^{0.5} = 35.43$ and CFL = 0.10.

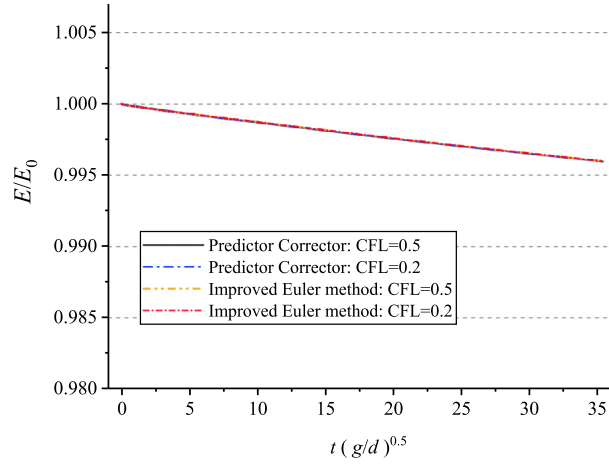


Fig. 7. Dissipation of total energy predicted by the present multi-phase SPH model with different time-integration schemes.

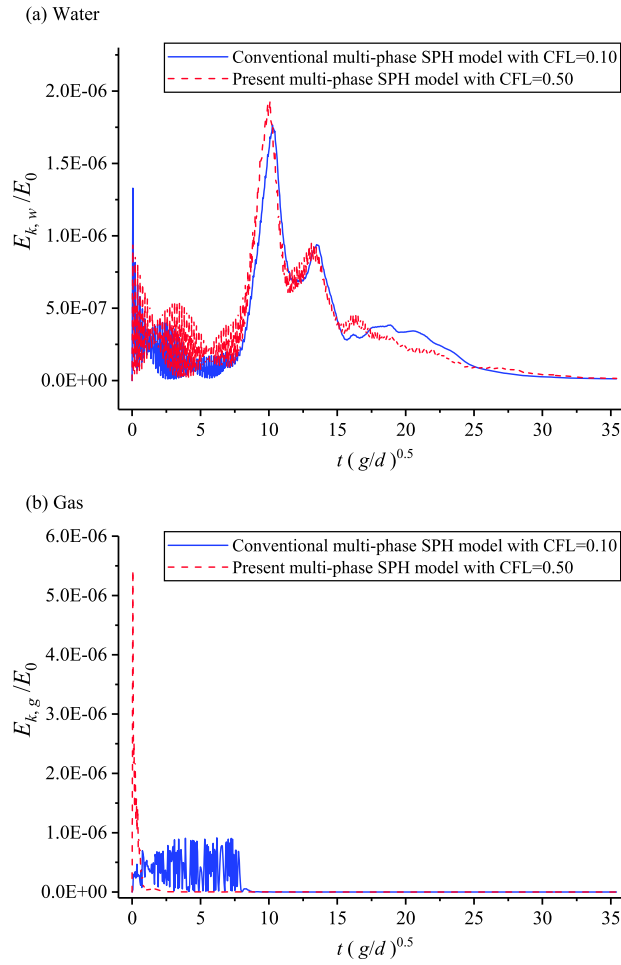


Fig. 8. Evolution of kinematic energy of two-phase hydrostatic water: (a) water; (b) gas.

presented in [55] were used as a benchmark to validate the proposed multi-phase SPH model for simulating free-surface flows. The numerical tank for the standing wave is similar to that for the hydrostatic water as shown in Fig. 4. Here, both the length L and height H of the tank are 2.0 m with the initial water depth $d = 1.0$ m. The artificial viscosity of water is

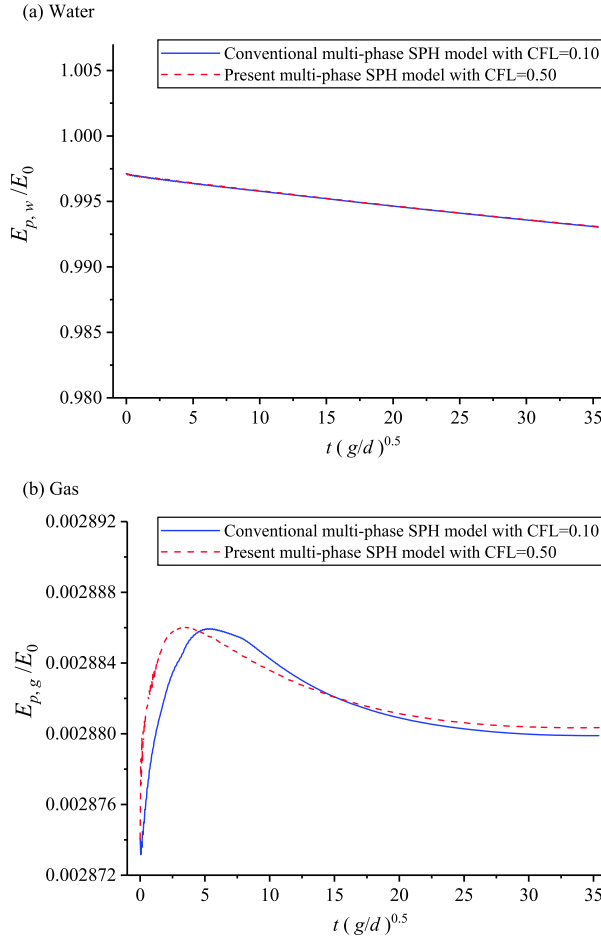


Fig. 9. Evolution of potential energy of two-phase hydrostatic water: (a) water; (b) gas.

adopted as $\alpha_w = 0.06$. Different from the hydrostatic water, the initial velocity potential of the standing wave is given by the following equation

$$\phi_0 = -\frac{Ag}{\sigma} \frac{\cosh[k(y+d)]}{\cosh(kd)} \cos(kx) \quad (48)$$

where A is the amplitude. $k = 2\pi/\lambda$ indicates the wave number. λ is the wave length that equals the tank length L . σ is the circular frequency given by the dispersion relation $\sigma^2 = gk \tanh(kd)$. It is noted that $y = 0$ denotes the position of the initial free surface and the initial condition (pressure and velocity distribution) of the standing wave is shown in Fig. 10.

The Reynolds number is a physical representation of the ratio of inertial forces to viscous forces, which is defined as

$$\text{Re} = \frac{d\sqrt{gd}}{\nu} \quad (49)$$

where ν is the numerical kinematic viscosity and theoretically given in two-dimension problem as [48]

$$\nu = \frac{\alpha c_0 h}{8} \quad (50)$$

with the smoothing length h and the artificial viscosity α .

Fig. 11 and Fig. 12 plot the evolution of kinematic energy predicted by the present multi-phase SPH model for the standing wave with $\text{Re}_w = 500$, $k = 2\pi$ and $A = 0.05$. It can be observed that the kinematic energy of water gradually attenuates as the prediction results by the linear solution of Antuono & Colagrossi [55]. With the CFL number decreasing from 0.50 to 0.20, the simulation results indicate that the present multi-phase SPH model has converged at CFL = 0.50, although there is a phase lag at the end of the attenuation. Meanwhile, the kinematic energy of water predicted by the present multi-phase SPH model still tends to the linear solution at the end of the attenuation with the increasing particle resolution in Fig. 12, demonstrating the good convergent performance of the present multi-phase SPH model in simulating

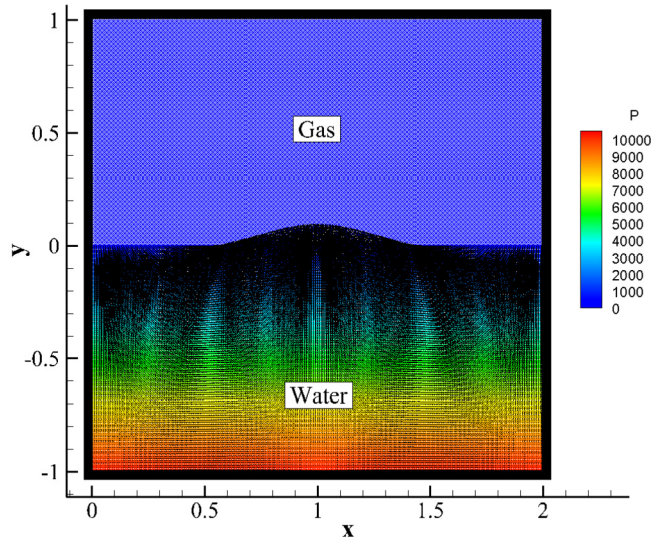


Fig. 10. The initial pressure and velocity distribution of the standing wave.

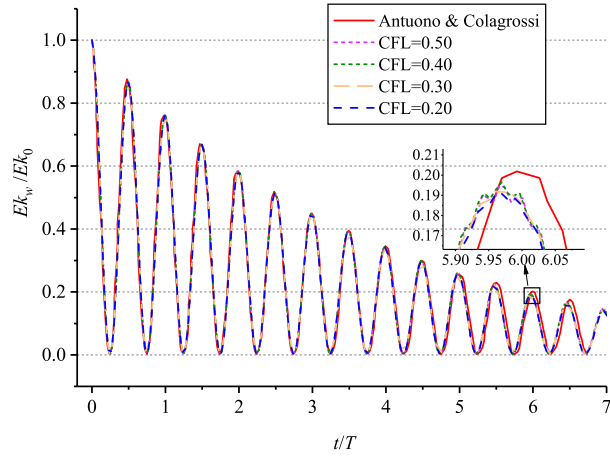


Fig. 11. Kinetic energy of water predicted by the linear solution (Antuono & Colagrossi [55]) and the present multi-phase SPH model with various CFL numbers and $L/dx = 200$ for the standing wave with $Re_w = 500$, $k = 2\pi$ and $A = 0.05$.

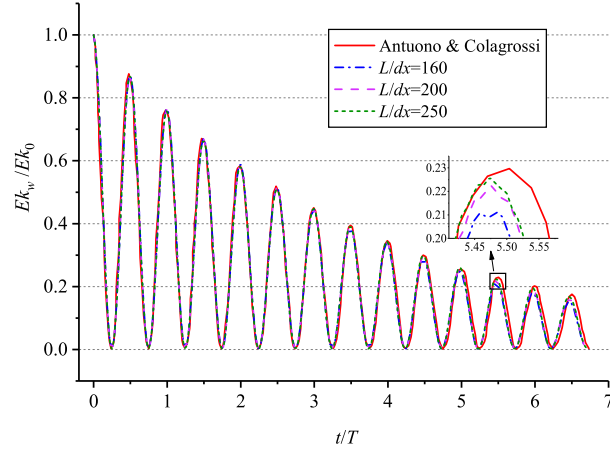


Fig. 12. Kinetic energy of water predicted by the linear solution (Antuono & Colagrossi [55]) and the present multi-phase SPH model with CFL = 0.20 and various L/dx for the standing wave with $Re_w = 500$, $k = 2\pi$ and $A = 0.05$.

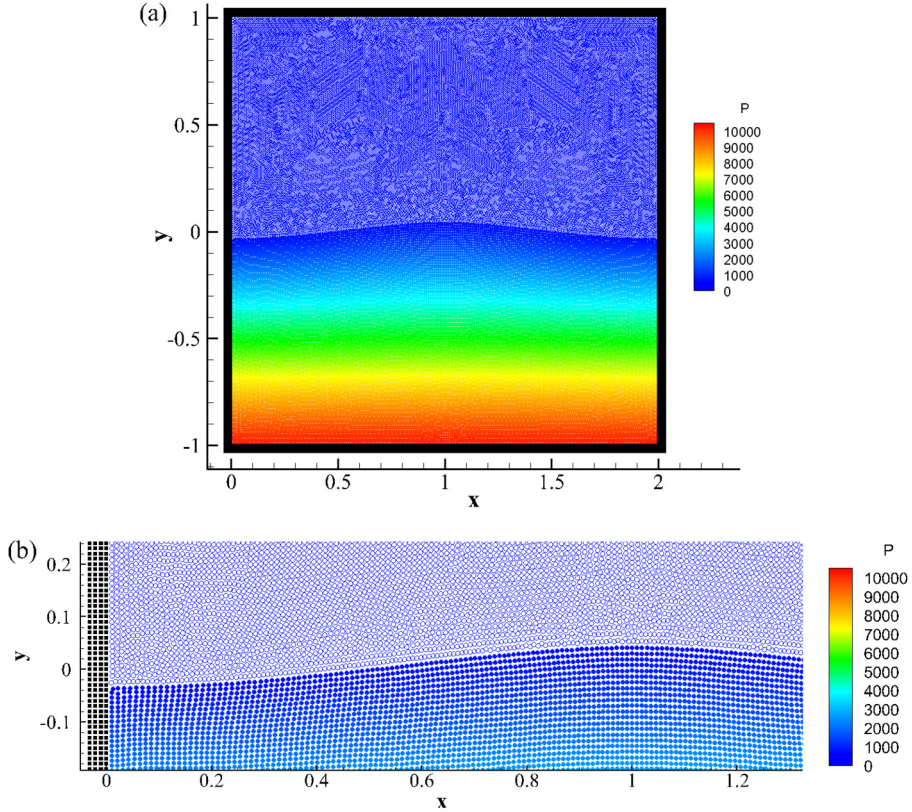


Fig. 13. Prediction by the present multi-phase SPH model at $t(g/d)^{0.5} = 8.02$ with $Re_w = 500$, $k = 2\pi$, $A = 0.05$, $L/dx = 200$ and $CFL = 0.20$: (a) pressure field; (b) zoom-in view of the multi-phase interface.

Table 1
Error estimation of the water velocity at the motionless instant by the present multi-phase SPH model for the standing wave with $Re_w = 500$, $CFL = 0.20$, $k = 2\pi$ and $A = 0.05$.

dx (m)	L/dx	N_w	$Error_{L_2}$ (m/s)
0.0125	160	12720	0.006
0.01	200	19900	0.00563
0.008	250	31125	0.00485
0.005	400	79800	0.00414

the multi-phase flows. Besides, Fig. 13 shows the pressure field predicted by the present multi-phase SPH model with $L/dx = 200$ and $CFL = 0.20$ at $t(g/d)^{0.5} = 8.02$. It can be seen that the pressure distribution is very smooth both in the same phase and across the multi-phase interface. In addition, the discernable multi-phase interface (see Fig. 13 (b)) further demonstrates that the proposed model can deal with the multi-phase interface with enough stability.

The L_2 norm of the water velocity is adopted as the error estimation. The L_2 norm of the water velocity is as follows:

$$Error_{L_2} = \|v_{numerical} - v_{theoretical}\|_{L_2} = \sqrt{\frac{\sum_{i=1}^{N_w} (v_{i,numerical} - v_{i,theoretical})^2}{N_w}} \quad (51)$$

where N_w is the total number of water particles.

There is a moment that all the particles of water are motionless when the standing wave moves to the highest or lowest position, so the velocity of the water particles is zero theoretically at that moment. Fig. 14 and Table 1 give the error estimation of the water velocity at the motionless instant predicted by the present multi-phase SPH model with $Re_w = 500$, $CFL = 0.20$, $k = 2\pi$ and $A = 0.05$. The error estimation of the water velocity decreases with the increase of the number of water particles. The error estimation of the water velocity is on the magnitude of $O(10^{-3})$ and the order of convergence about 0.668 can be obtained, which indicates that the total water particles are close to being motionless compared to the initial averaged velocity on the magnitude of $O(10^{-1})$. In fact, the water particles cannot be absolutely static due to the numerical error. The results demonstrate that the present multi-phase SPH performs well on the convergence.

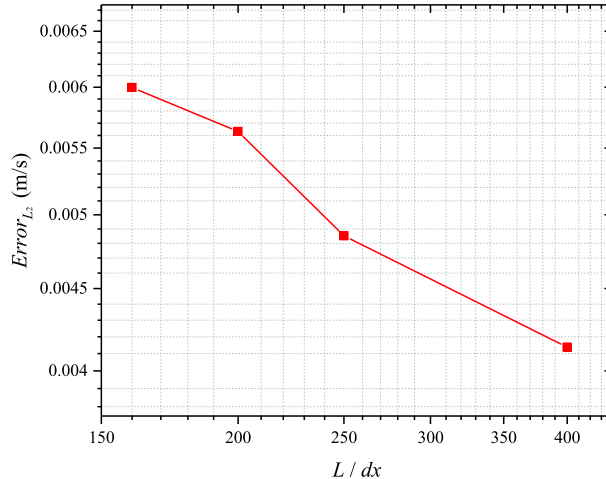


Fig. 14. Error estimation of the water velocity at the motionless instant by the present multi-phase SPH model for the standing wave with $Re_w = 500$, $CFL = 0.20$, $k = 2\pi$ and $A = 0.05$.

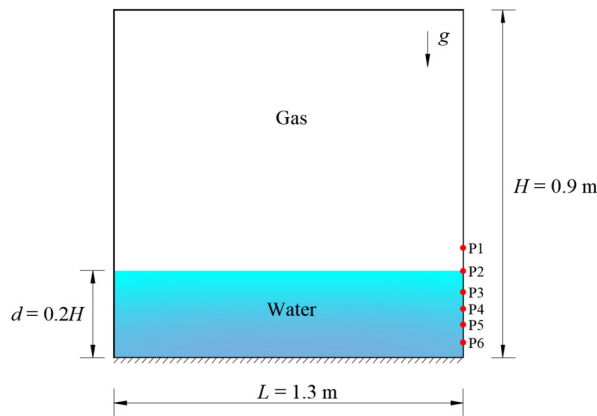


Fig. 15. Schematic diagram of two-phase liquid sloshing setup.

4.3. Two-phase liquid sloshing

The phenomenon of liquid movement in a partially filled moving tank is known as liquid sloshing. When the external frequency of the tank movement is close to the natural frequency of the sloshing liquid inside, a resonance condition of the sloshing occurs. This resonance relates to the complex movement of the filled liquid, which may be coupled with the structure movement. Due to the highly non-linear phenomena, liquid sloshing has been widely used as a testing example in SPH simulations [44,56–59]. In this subsection, the experiment of liquid sloshing [60] is used as a benchmark to validate the stability and accuracy of the present multi-phase SPH model.

The schematic of the two-phase liquid sloshing problem is shown in Fig. 15. The length L and height H of the tank are 1.3 m and 0.9 m, respectively. The tank is partially filled with water with the water depth $d = 0.2H = 0.18$ m. The tank is motivated by a sinusoidal motion $x = A \sin(2\pi ft)$, where $A = 0.10$ m and $f = 0.496$ Hz are the amplitude and frequency of the sinusoidal motion, respectively. It is noted that the frequency $f = 0.496$ Hz is close to the resonance frequency of the filled water [60], which would result in violent sloshing. Hence, we adopt the boundary force to the water particle here to avoid penetrating due to the violent sloshing. Besides, density reinitialization [61] is used in this case to improve the mass-area-density consistency. As shown in Fig. 15, six pressure sensors P1-P6 are installed at the right side of the tank, and their positions are 0.195 m, 0.180 m, 0.165 m, 0.135 m, 0.120 m and 0.105 m away from the bottom, respectively. Specifically, P2 is on the free surface, P1 is on the upside, and the others are below the initial water level.

Fig. 16 plots the liquid sloshing evolution at different instants simulated by the present multi-phase SPH model with $L/dx = 260$. It is noted that the tank is reverted to the initial position for comparison. It is observed that the periodic movement of the tank wall results in high flow nonlinearity. The water strongly impacts the tank wall, leading to the large deformed free surface and the splash. The multi-phase interface is well maintained without unphysical phase separation even though the resonance happens. Fig. 17 enlarges the view of the velocity vector and pressure field for liquid sloshing

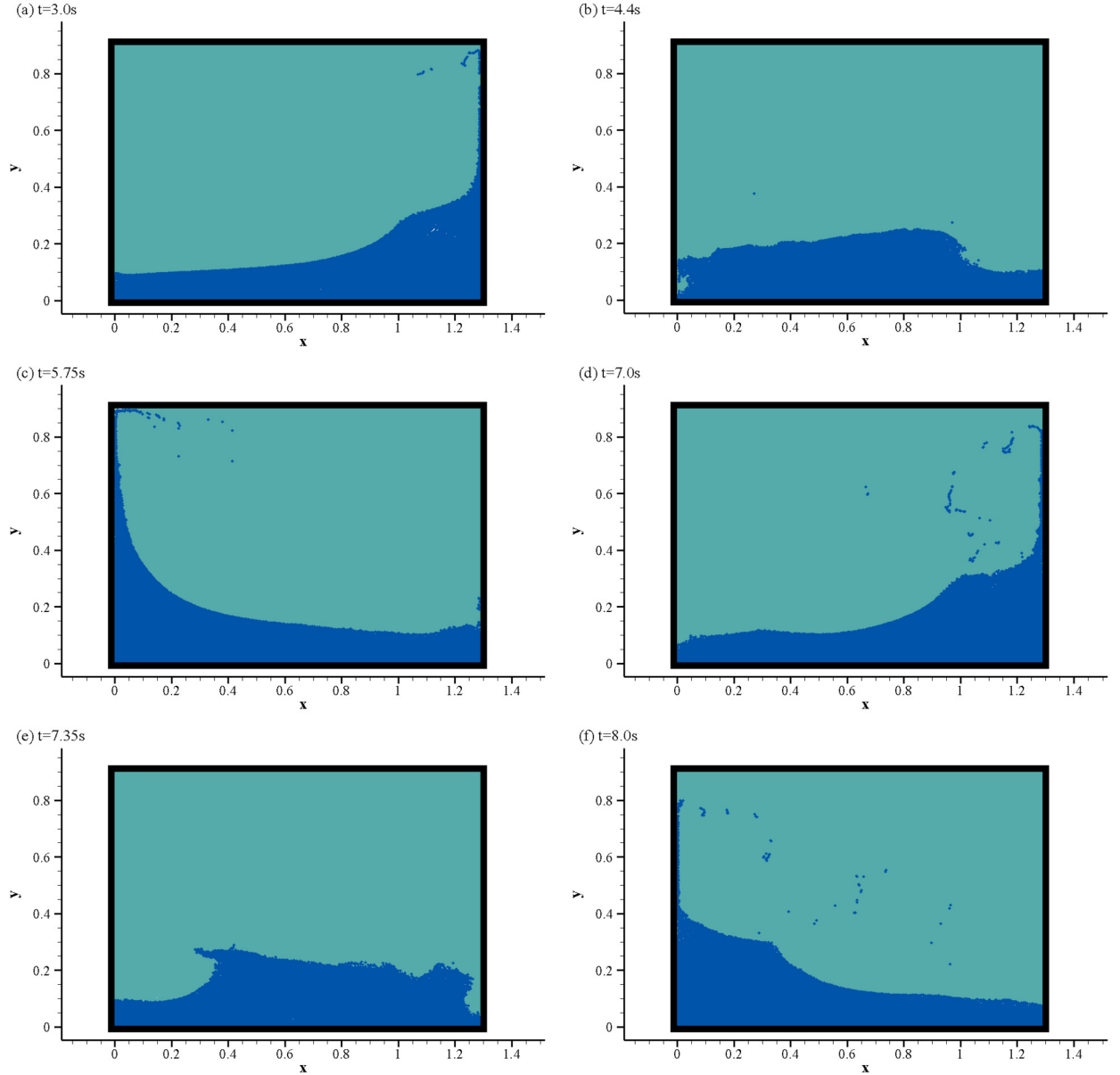


Fig. 16. Snapshots of the liquid sloshing predicted by the present multi-phase SPH model with $L/dx = 260$ at different time instants: (a) $t = 3.0\text{ s}$; (b) $t = 4.4\text{ s}$; (c) $t = 5.75\text{ s}$; (d) $t = 7.0\text{ s}$; (e) $t = 7.35\text{ s}$; and (e) $t = 8.0\text{ s}$.

at 4.4 s and 7.0 s. In contrast to that shown in [44] where the gas velocity vectors are radiated and disordered, the velocity predicted by the present multi-phase model is continuous and smooth even across the phase interfaces.

Fig. 18 records the time history of the pressure at the sensors P1-P6 in comparison with the experimental results in Rafiee et al. [60] and the multi-phase SPH predictions in Rezavand et al. [44]. The present multi-phase SPH model obtains a good agreement with the reference results. An increase in the resolution improves the computing accuracy of the peak pressure value, e.g., for P2 and P4. Though there are some discrepancies on the peak value of pressure especially for P3, the present multi-phase SPH model has a similar performance with the multi-phase SPH model by Rezavand et al. [44], e.g., for P1, P2 and P3. Besides, it can be observed that the pressure values predicted by the present multi-phase SPH model at P4, P5 and P6 are slightly higher than the experimental data, but they are in the almost same trends. The small difference between simulations and experiments is considered to come from the ignorance of three-dimensional features in the simulations weakening the violent flow below the initial water level. In general, the liquid sloshing simulations demonstrate that the present multi-phase SPH model overcomes the stability problem at the multi-phase interface. It has better kinematic and dynamic characteristics with enough accuracy in violent flows.

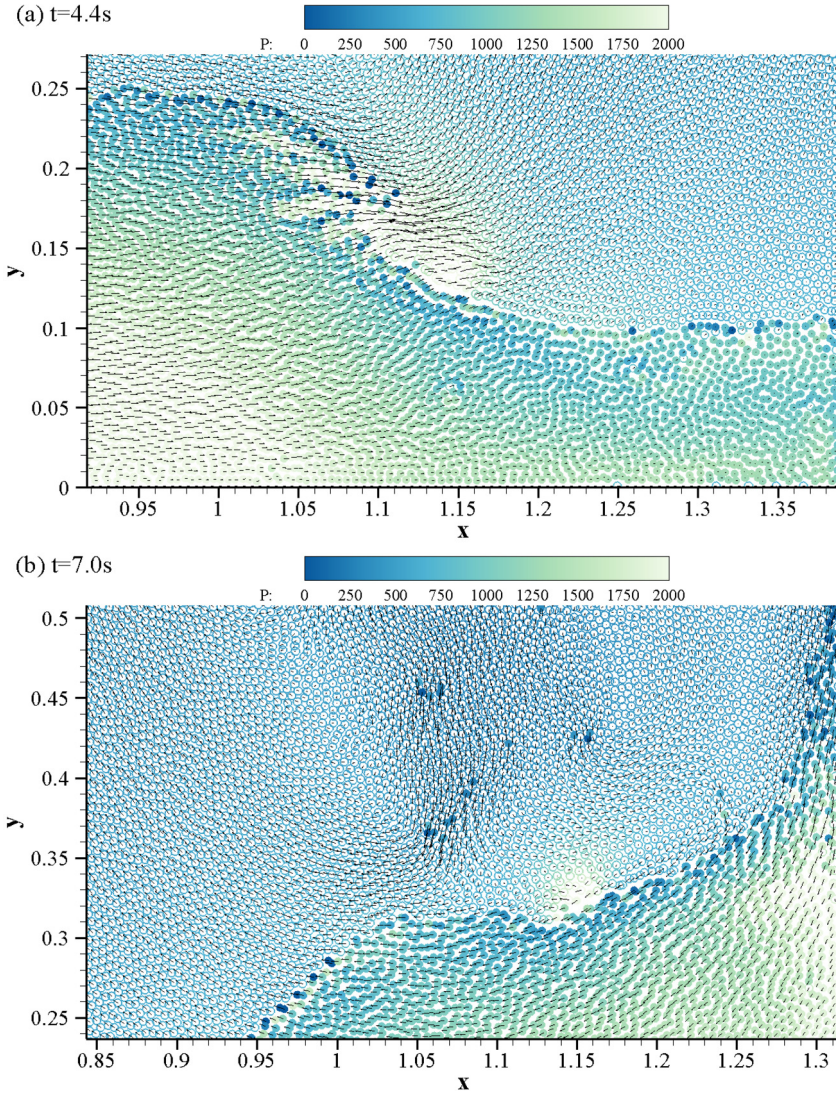


Fig. 17. Zoom-in view of the velocity vector and pressure field: (a) $t = 4.4$ s; and (b) $t = 7.0$ s.

4.4. Two-phase dam breaking

The dam breaking involves the complex impacts, surface breakage, jet flow, and other violent phenomena. It brings a great challenge for the numerical solvers and has been widely used to validate the SPH-related numerical methods, e.g., in [34,44,62–64]. Lobovský et al. [65] carried out a series of experimental tests for the dam breaking, provided detailed wave front motion and impact pressure data, and recorded the snapshots of the free surfaces' evolution. We use one experimental case in [65] as a benchmark here to further test the stability and accuracy of the present multi-phase SPH model for simulating the violent flows.

Fig. 19 illustrates a schematic diagram of the numerical flume of the dam breaking test. The length of the numerical flume is $L = 1610$ mm, the height is $D = 600$ mm, the bottom width of the water body in the dam is $l = 600$ mm, and there is a 1010-mm-long barrier-free horizontal bottom bed at the downstream side of the dam body. The water depth in the dam is d . There are four measuring points H1, H2, H3 and H4 for the water level elevation inside the numerical flume. H1 is located in the middle of the water body in the dam. H2, H3 and H4 are 265 mm, 514 mm and 763 mm away from the initial front face of the dam body, respectively. Four pressure sensors #1, #2, #3 and #4 are set on the downstream wall of the numerical flume. Their center points are 3 mm, 15 mm, 30 mm and 80 mm away from the bottom of the numerical flume, respectively. The acquisition frequencies of the measuring points of water level elevation and the pressure sensors are all 100 Hz.

In the dam breaking case, the water depth is set as $d = 0.30$ m, the initial particle spacing is adopted as $dx = 5$ mm, and the numerical sound speed is adopted as $c_0 = 50.0$ m/s. Meanwhile, we use the density reinitialization in [61] to

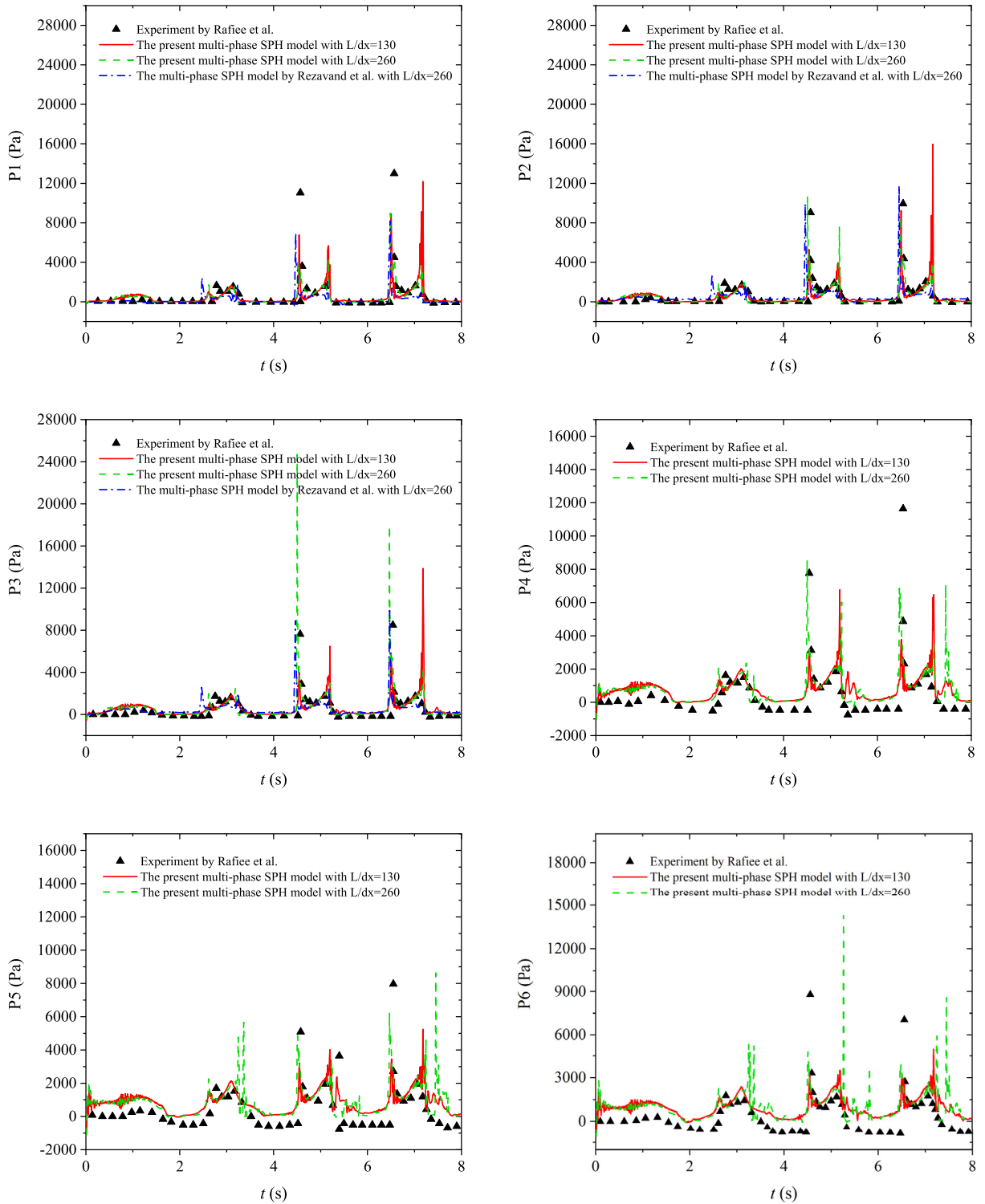


Fig. 18. Impact pressure evolution at P1-P6 in comparison with experimental data in Rafiee et al. [60] and multi-phase SPH predictions in Rezavand et al. [44].

improve the mass-area-density consistency. Considering that Lobovský et al. [65] conducted the dam breaking test by the dam gate release system, the release of the dam gate has an effect on the hydrostatic pressure distribution in the dam body.

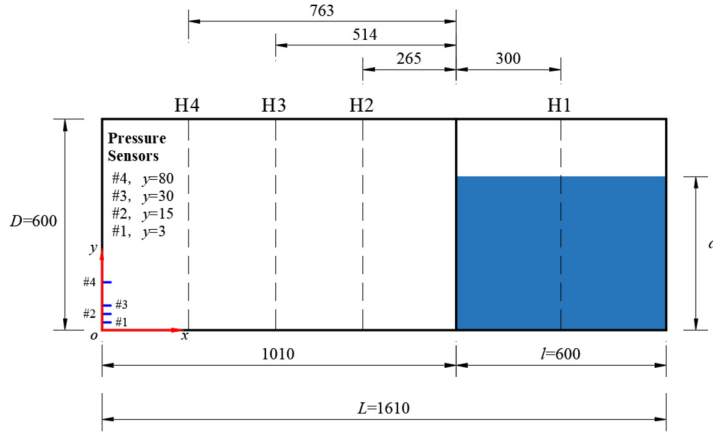


Fig. 19. Sketch of the dam breaking configuration.

To eliminate such effect, the initial pressure distribution in the water body is set by using the semi-infinite dam hydrostatic pressure distribution in [64] as

$$p_0(x, y) = p_b + \rho_{0,w} g (d - y) - \frac{8\rho_w g d}{\pi^2} \sum_{n=0}^{\infty} \left\{ \frac{1}{(2n+1)^2} e^{\frac{(2n+1)\pi(L-l-x)}{2d}} \cos\left(\frac{2n+1}{2d}\right) \pi y \right\} \quad (52)$$

where $p_0(x, y)$ indicates the initial pressure distribution in the water body. The coordinate system xOy is set at the left bottom corner as shown in Fig. 19.

4.4.1. 2D dam breaking

4.4.1.1. Kinematic characteristics Fig. 20 illustrates the snapshots of the dam breaking evolution after releasing the dam gate. It is noted that the black dash dot depicts the multi-phase interface. At the early stage, the generated primary wave propagates downstream and eventually hits the wall, causing a large vertical run-up jet. After that, the reflected wave develops into a plunging breaker. It can be observed that the multi-phase interface predicted by the present multi-phase SPH model keeps clear and smooth all the way. Although a few solitary water particles' pressure around the multi-phase interface is larger than the surrounding particles, as shown in Fig. 20 (d) and (e), the entire pressure field still keeps continuous and smooth. In particular, the dam breaking process produced by present method is always consistent with the experimental observations without evident non-physical voids in both the gas and water phases.

In this case, the wave front indicates the front part of the primary wave. The position evolution of the wave front over time is shown in Fig. 21. It can be observed that the velocity of the wave front gradually increases with the dam breaking development until the primary wave hits the downstream wall. At the early stage of the dam breaking, the wave front velocity predicted by the numerical simulations is slower than the experimental data, then the wave front gradually speeds up, and finally hits the downstream wall slightly earlier than the experimental observation. Through our comparison, it can be observed that the prediction by the proposed multi-phase SPH model is closer to the experimental data than the single-phase SPH model.

Fig. 22 shows the evolution of the water level elevation at H1-H4. The water level elevation at H1 gradually decreases with the dam breaking development. It is not difficult to find that the present simulation results are consistent with the experimental test results. In general, the numerical results of the water level elevation at measuring point H1 are slightly faster than the experimental test results, but on the whole they are close to the experimental test results.

The water level measuring points at H2, H3 and H4 are located in the downstream direction of the dam body, and there are two jumps at these water level elevations as shown in Fig. 22. The first jump happens when the primary wave reaches the water level measuring point, and the second jump occurs when the reflected wave reaches the water level measuring point again. It is found from the comparison that the numerical simulation results before the second jump are in good agreement with the experimental observation. Though there are some differences between the numerical simulation results and the experimental result after the second jump, the water level elevations at H2, H3, and H4 predicted by the present multi-phase SPH model with $CFL = 0.20$ are still similar to the conventional multi-phase SPH model with $CFL = 0.10$.

4.4.1.2. Dynamic characteristic The primary wave of the dam breaking hits the downstream wall, resulting in huge impact pressure and complex water flow structure. The evolutions of the pressure at sensors #1, #2, #3 and #4 are presented in Fig. 23. The pressure predicted by numerical simulations at #3 and #4 agrees well with the experimental test. However, there are some differences in the pressure's peak values at #1 and #2. It can be seen that the pressure predicted by

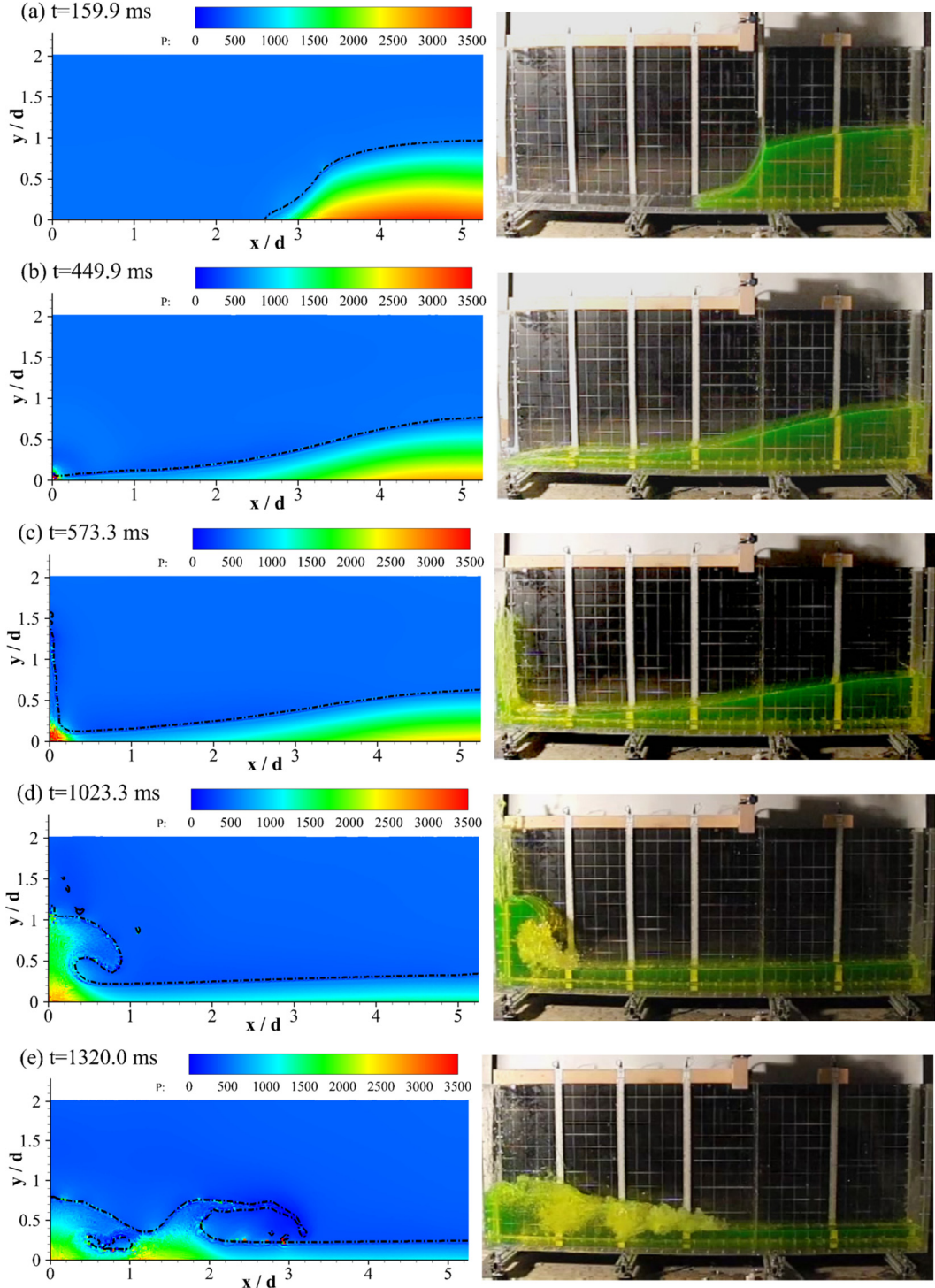


Fig. 20. Snapshots of the dam breaking at (a) $t = 159.9$ ms; (b) $t = 449.9$ ms; (c) $t = 573.3$ ms; (d) $t = 1023.3$ ms; and (e) $t = 1320.0$ ms. Left: the present multi-phase SPH model at CFL = 0.20; right: Lobovský et al. [65].

both the single-phase SPH model and the conventional multi-phase model with CFL = 0.20 at #1 significantly exceeds the experimental test result. In comparison, the present multi-phase SPH model with CFL = 0.20 has better results at #1 that is close to the conventional multi-phase SPH model with smaller CFL = 0.10. Though the pressure predicted by the present multi-phase SPH model with CFL = 0.20 also reaches a peak pressure at #2 as twice the experimental test, the present

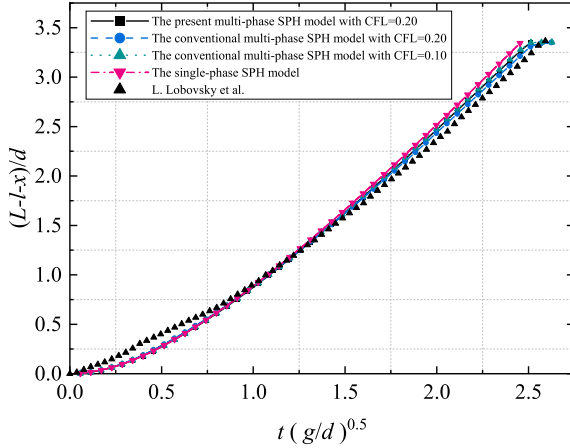


Fig. 21. Evolution of the downstream wave front against experimental data in Lobovský et al. [65].

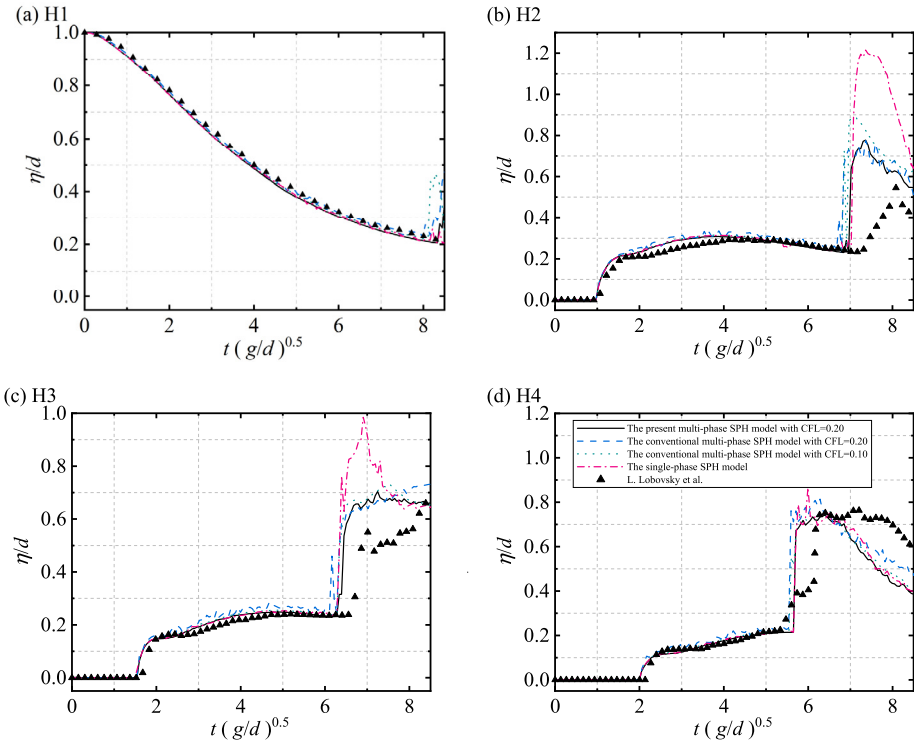


Fig. 22. Evolutions of the water level elevations against experimental data in Lobovský et al. [65] at (a) H1; (b) H2; (c) H3; and (d) H4.

multi-phase SPH model with $CFL = 0.20$ keeps a consistent trend with the experimental data. The too-large peak pressure may be caused by the too-small distance between sensors and the flume bottom.

Fig. 24 shows the snapshot of the dam breaking simulation at $t(g/d)^{0.5} = 7.32$, where the reflected wave hits the free surface and then results in the water splashing. As shown in Fig. 24 (b), it is observed that the gas pressure near the multi-phase interface predicted by the conventional multi-phase SPH model with $CFL = 0.20$ becomes too large so that the huge pressure oscillations break the continuous pressure field near the interface. As shown in Fig. 24 (a) and (c), the pressure field predicted by the present multi-phase SPH model with $CFL = 0.20$ and the conventional multi-phase SPH model with smaller $CFL = 0.10$ is able to keep light oscillations that have a negligible influence on the numerical stability.

Fig. 25 shows the zoom-in view of the velocity field of the gas cavity at $t(g/d)^{0.5} = 7.32$. It can be observed that the gas cavity is surrounded by the plunging wave. The velocity field predicted by the present multi-phase SPH model with $CFL = 0.20$ (see Fig. 25 (a\|b-1)) is smooth and continuous both inside the phases (water or gas) and across the multi-phase interface, which is similar to the conventional multi-phase SPH model with smaller $CFL = 0.10$ (see Fig. 25

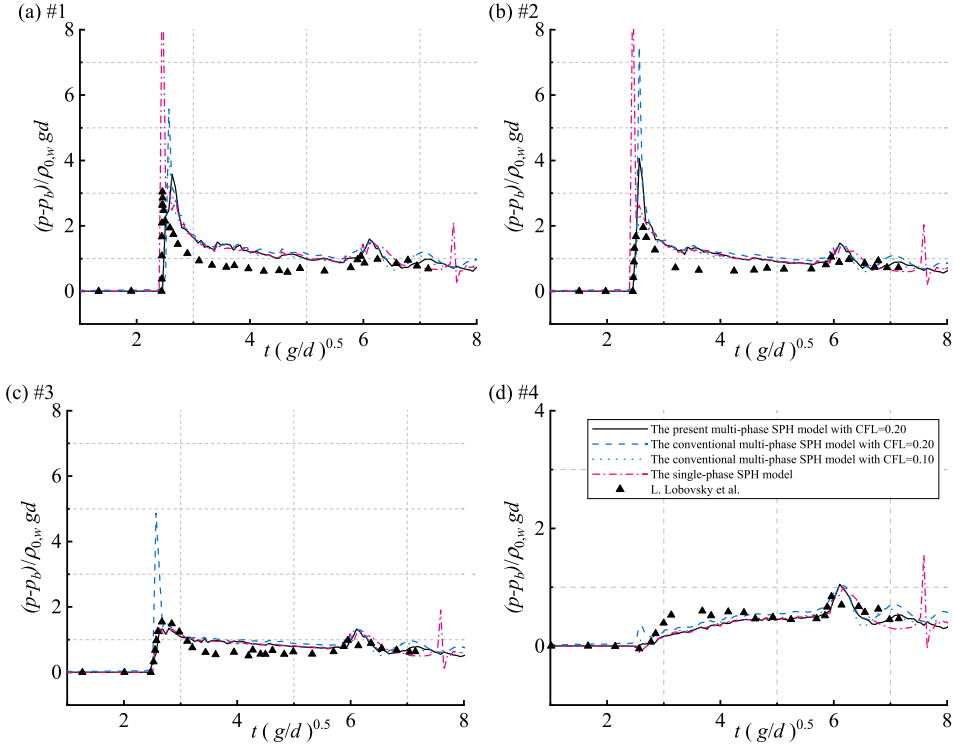


Fig. 23. Pressure evolution against experimental data in Lobovský et al. [65] at (a) #1; (b) #2; (c) #3; and (d) #4.

(a\b-3)). Meanwhile, the gas velocity has the same magnitude as the water. In contrast, the velocity field predicted by the conventional multi-phase SPH model with $CFL = 0.20$ (see Fig. 25 (a\b-2)) is disordered and unsmooth across the multi-phase interfaces. The unstable velocity field and the huge pressure oscillations near the multi-phase interface result in the simulation termination of the conventional multi-phase SPH model with $CFL = 0.20$ at the later stage ($t(g/d)^{0.5} = 12.12$). In addition, the free surface at $t(g/d)^{0.5} = 7.32$ is compared in Fig. 26. We can find that the free surfaces predicted by all of these three models are similar, but as a matter of fact the free surface predicted by the present multi-phase SPH model with $CFL = 0.20$ can reach the same level by the conventional multi-phase SPH model at smaller $CFL = 0.10$. Therefore, it can be further demonstrated that the present multi-phase SPH model has advantages in stability and accuracy with a higher CFL number than the conventional multi-phase SPH model.

4.4.2. 3D dam breaking

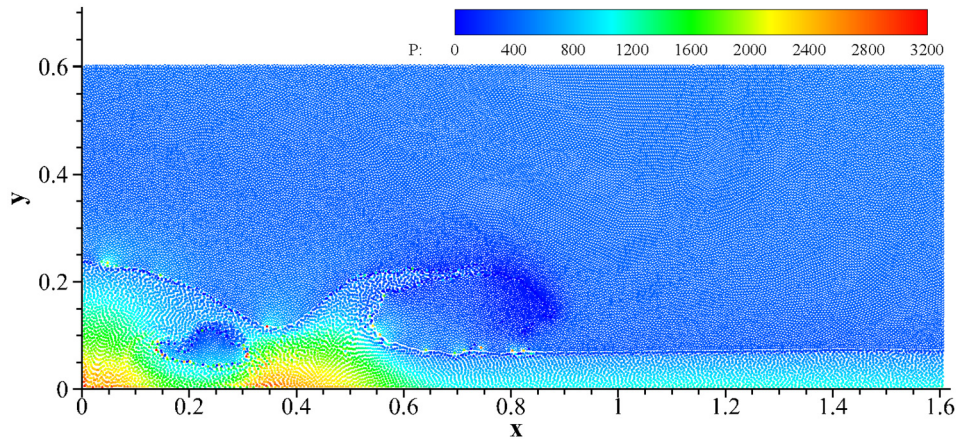
To demonstrate the effectiveness of the new multiphase SPH model in simulating 3D problems, we also extended the dam breaking problem from 2D to 3D. The flume width in the 3D simulation is 150 mm. The initial particle spacing is also adopted as $dx = 5$ mm, which makes the number of total particles up to 1558144. The other numerical parameters in 3D simulation are consistent with those in 2D simulation. The computational cost for the simulation of 3D multi-phase dam breaking is too huge to be executed by a serial program. In order to reduce the cost of computational time, on the one hand, a larger $CFL = 0.50$ is applied into 3D simulation; on the other hand, the parallelization technology by GPU (Graphics Processing Unit) implementation is used to accelerate the computation.

Fig. 27 shows the evolution of 3D dam breaking predicted by the present multi-phase SPH model. The results indicate that the present multi-phase SPH model also has the ability to maintain a stable interface and obtain the smooth flow field in the 3D multi-phase violent flow. The results for the simulation of 3D dam breaking further confirm the advantage of the present multi-phase SPH model for simulations of violent flows in the acceptable CFL number and the numerical stability.

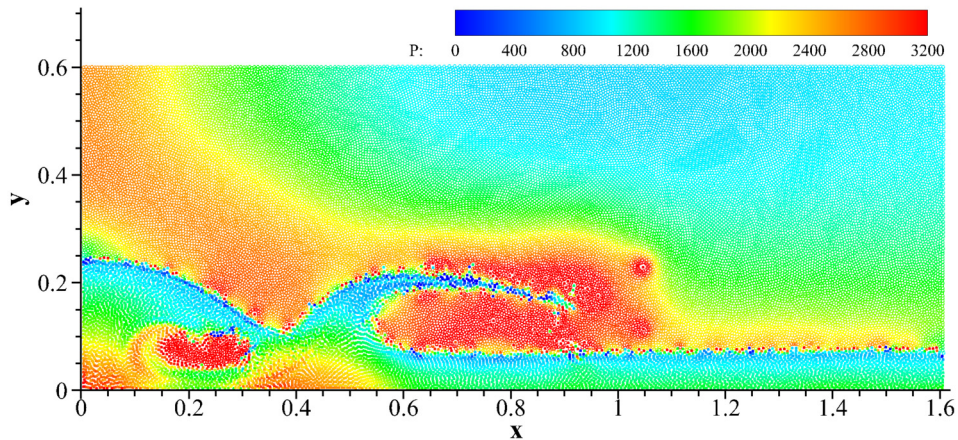
5. Conclusion

The SPH method is attractive in modeling multi-phase flows with moving interfaces, and many previous works usually involve the summation density approach to approximate density. The continuity density approach is of great potential to approximate density in the simulation of multi-phase flows because the time-rate density variation closely relates to the compressibility and energy variation of the fluids. However, the conventional multi-phase SPH model is usually associated with poor accuracy and, more importantly, a small CFL number for large density ratios. In this work, we propose a fully weakly-compressible SPH model for simulating multi-phase flows with large density ratios. The main idea of the present

(a) The present multi-phase SPH model with CFL=0.20



(b) The conventional multi-phase SPH model with CFL=0.20



(c) The conventional multi-phase SPH model with CFL=0.10

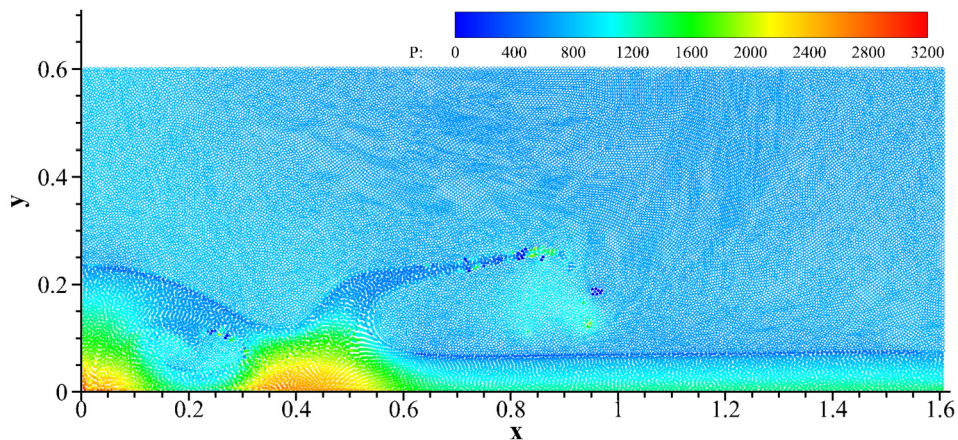


Fig. 24. Snapshots of dam breaking simulations at $t(g/d)^{0.5} = 7.32$ by (a) the present multi-phase SPH model with $CFL = 0.20$; (b) the conventional multi-phase SPH model with $CFL = 0.20$; and (c) the conventional multi-phase SPH model with $CFL = 0.10$.

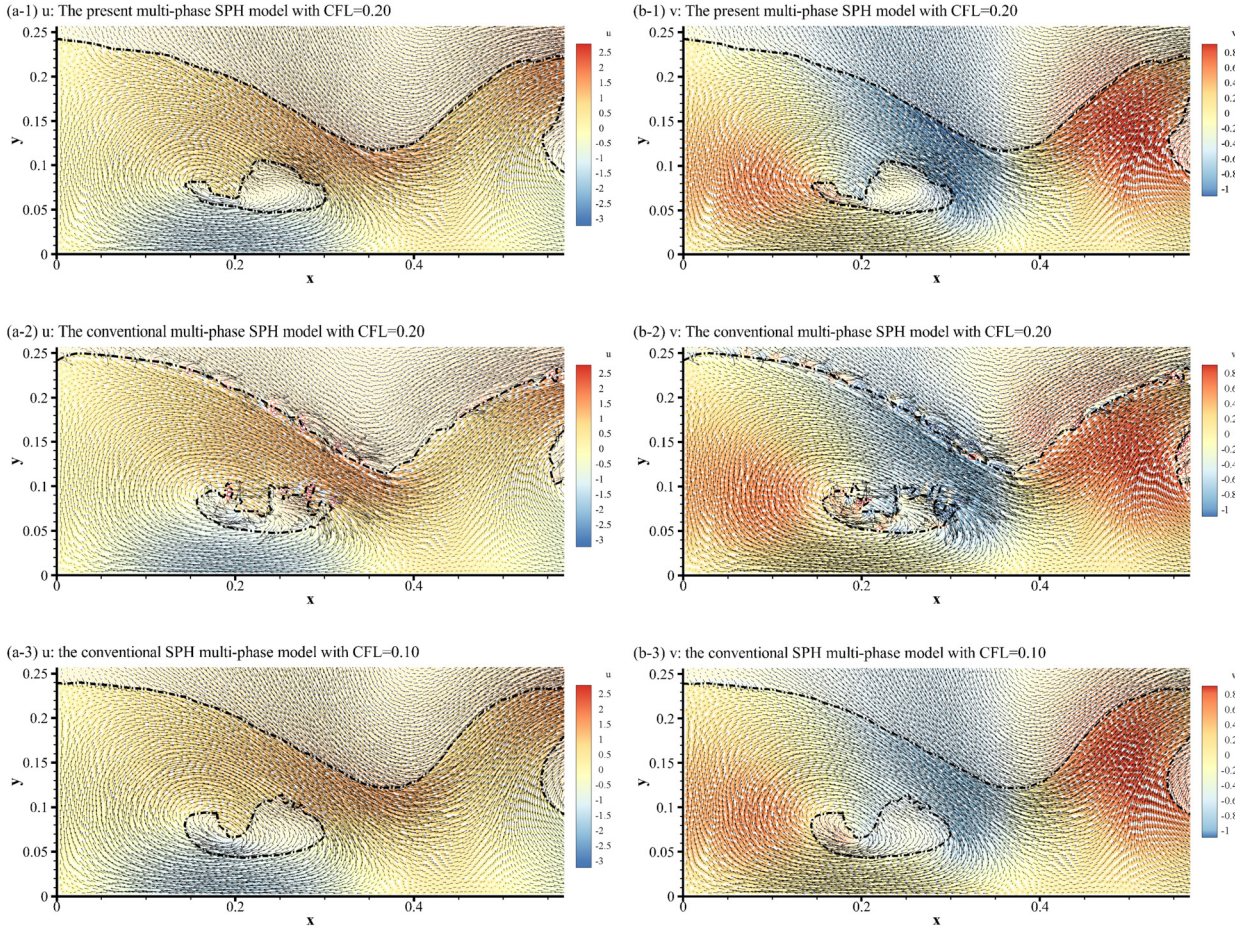


Fig. 25. Zoom-in view of the velocity field of the gas cavity at $t(g/d)^{0.5} = 7.32$ for (a-1) x -direction velocity u by the present multi-phase SPH model with $CFL = 0.20$; (a-2) x -direction velocity u by the conventional multi-phase SPH model with $CFL = 0.20$; (a-3) x -direction velocity u by the conventional multi-phase SPH model with $CFL = 0.10$; (b-1) y -direction velocity v by the present multi-phase SPH model with $CFL = 0.20$; and (b-2) y -direction velocity v by the conventional multi-phase SPH model with $CFL = 0.20$, and (b-3) y -direction velocity v by the conventional multi-phase SPH model with $CFL = 0.10$.

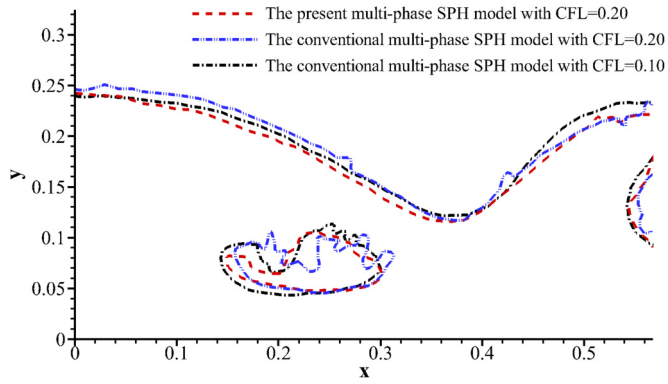


Fig. 26. Zoom-in view of the free surface at $t(g/d)^{0.5} = 7.32$.

multi-phase model is to approximate the continuity equation over neighboring particles of the same phase, and to re-initialize the pressure and density of the interacting particles of the other phase based on the Shepard kernel. Besides, the fluid information of boundary particles is updated by a very accurate and careful process.

Four two-phase flow problems, including hydrostatic water, standing wave, liquid sloshing and dam breaking, are tested to validate the present SPH model for simulating the multi-phase flows with large density ratios and moving interfaces.

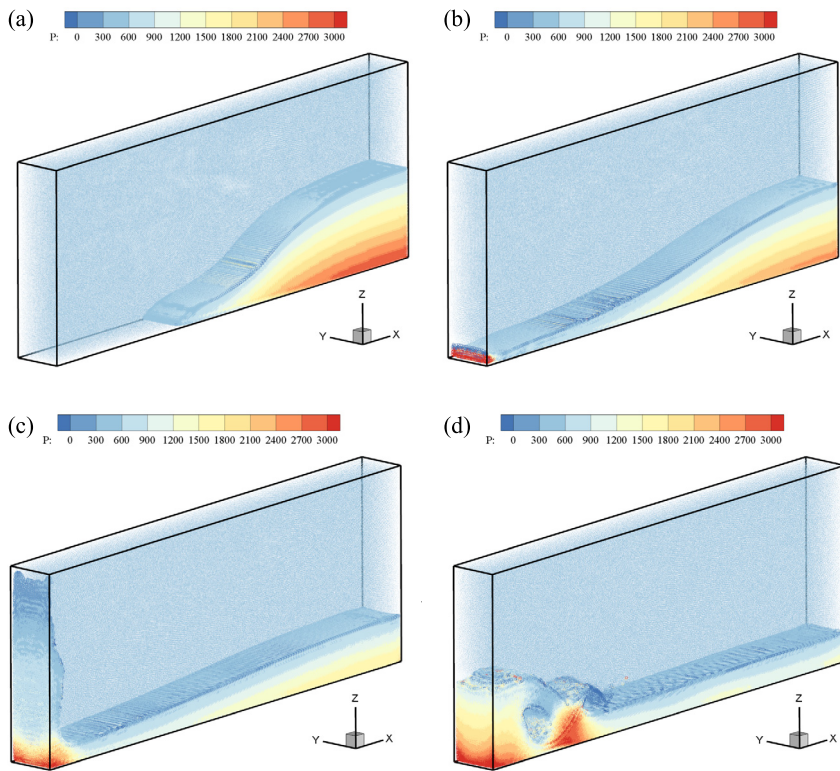


Fig. 27. Evolution of 3D dam breaking predicted by the present multi-phase SPH model at (a) $t = 250$ ms; (b) $t = 450$ ms; (c) $t = 750$ ms; (d) $t = 1100$ ms.

It has been demonstrated that the proposed novel multi-phase SPH model has good accuracy with smooth pressure field and continuous phase interface. More importantly, larger CFL numbers can be used in the present multi-phase SPH model, which can significantly save computational efforts through larger time steps.

CRediT authorship contribution statement

Fang He: Conceptualization, Formal analysis, Investigation, Supervision, Writing – review & editing. **Huashan Zhang:** Formal analysis, Methodology, Software, Writing – original draft. **Can Huang:** Investigation, Methodology, Visualization, Writing – review & editing. **Moubin Liu:** Supervision, Writing – review & editing.

Declaration of competing interest

The authors declare that they have no known competing financial interests or personal relationships that could have appeared to influence the work reported in this paper.

Acknowledgements

This work was supported by the National Natural Science Foundation of China (Nos. 52022092, 51979247, 12002002 and 12032002), Fundamental Research Funds for the Central Universities (No. 2020QNA4043), Fundamental Research Funds for Beijing Municipal Universities, the Launching Scientific Research Funds of North China University of Technology and HPC Center of ZJU (Zhoushan Campus).

References

- [1] B. Aboulhasanzadeh, S. Thomas, M. Taeibi-Rahni, G. Tryggvason, Multiscale computations of mass transfer from buoyant bubbles, *Chem. Eng. Sci.* 75 (2012) 456–467.
- [2] B. Attiya, M. Altimemy, J. Caspar, C. Daskiran, I.H. Liu, A. Oztekin, Large eddy simulations of multiphase flows past a finite plate near a free surface, *Ocean Eng.* 188 (2019) 106342.
- [3] M. Sussman, A level set approach for computing solutions to incompressible two-phase flow, *J. Comput. Phys.* 114 (1994) 146–159.
- [4] L. Fu, X.Y. Hu, N.A. Adams, Single-step reinitialization and extending algorithms for level-set based multi-phase flow simulations, *Comput. Phys. Commun.* 221 (2017) 63–80.

- [5] F.S. Schranner, X.Y. Hu, N.A. Adams, On the convergence of the weakly compressible sharp-interface method for two-phase flows, *J. Comput. Phys.* 324 (2016) 94–114.
- [6] G. Tryggvason, B. Bunner, A. Esmaeeli, D. Juric, N. Al-Rawahi, W. Tauber, J. Han, S. Nas, Y.J. Jan, A front-tracking method for the computations of multiphase flow, *J. Comput. Phys.* 169 (2001) 708–759.
- [7] A. Hasečić, S. Muzaferija, I. Demirdžić, Finite volume method for multiphase flows with radiation and phase change, *Int. J. Therm. Sci.* 149 (2020) 106201.
- [8] X. Fan, A. Salama, S. Sun, A locally and globally phase-wise mass conservative numerical algorithm for the two-phase immiscible flow problems in porous media, *Comput. Geotech.* 119 (2020).
- [9] P. Salinas, D. Pavlidis, Z. Xie, H. Osman, C.C. Pain, M.D. Jackson, A discontinuous control volume finite element method for multi-phase flow in heterogeneous porous media, *J. Comput. Phys.* 352 (2018) 602–614.
- [10] M.K. Li, A.M. Zhang, F.R. Ming, P.N. Sun, Y.X. Peng, An axisymmetric multiphase SPH model for the simulation of rising bubble, *Comput. Methods Appl. Mech. Eng.* 366 (2020).
- [11] T. Jiang, Y. Li, P.N. Sun, J.L. Ren, Q. Li, J.Y. Yuan, A corrected WCSPH scheme with improved interface treatments for the viscous/viscoelastic two-phase flows, *Comput. Part. Mech.* (2021).
- [12] T. Jiang, J. Ren, J. Yuan, W. Zhou, D.-S. Wang, A least-squares particle model with other techniques for 2D viscoelastic fluid/free surface flow, *J. Comput. Phys.* 407 (2020) 109255.
- [13] S. Lee, K. Ko, J.W. Hong, Comparative study on the breaking waves by a piston-type wavemaker in experiments and SPH simulations, *Coast. Eng. Jpn.* 62 (2020) 267–284.
- [14] D. Chen, W. Huang, A. Lyamin, Finite particle method for static deformation problems solved using JFNK method, *Comput. Geotech.* 122 (2020).
- [15] Z.L. Zhang, M.B. Liu, Numerical studies on explosive welding with ANFO by using a density adaptive SPH method, *J. Manuf. Process.* 41 (2019) 208–220.
- [16] M.B. Liu, Z.L. Zhang, D.L. Feng, A density-adaptive SPH method with kernel gradient correction for modeling explosive welding, *Comput. Mech.* 60 (2017) 513–529.
- [17] A. Khayyer, H. Gotoh, H. Falahaty, Y. Shimizu, An enhanced ISPH-SPH coupled method for simulation of incompressible fluid–elastic structure interactions, *Comput. Phys. Commun.* 232 (2018) 139–164.
- [18] Y. Shi, S. Li, S. Peng, H. Chen, M. He, Numerical modeling of flexible floating boom using a coupled SPH-FEM model, *Coast. Eng. Jpn.* 60 (2018) 140–158.
- [19] X. Zheng, X. Lv, Q. Ma, W. Duan, A. Khayyer, S. Shao, An improved solid boundary treatment for wave–float interactions using ISPH method, *Int. J. Nav. Archit. Ocean Eng.* 10 (2018) 329–347.
- [20] L. Han, X.Y. Hu, SPH modeling of fluid-structure interaction, *J. Hydromech.* 30 (2018) 62–69.
- [21] P. Sun, A.M. Zhang, S. Marrone, F. Ming, An accurate and efficient SPH modeling of the water entry of circular cylinders, *Appl. Ocean Res.* 72 (2018) 60–75.
- [22] A. Khayyer, H. Gotoh, Y. Shimizu, K. Gotoh, H. Falahaty, S. Shao, Development of a projection-based SPH method for numerical wave flume with porous media of variable porosity, *Coast. Eng.* 140 (2018) 1–22.
- [23] H. Wen, B. Ren, P. Dong, G. Zhu, Numerical analysis of wave-induced current within the inhomogeneous coral reef using a refined SPH model, *Coast. Eng.* 156 (2020).
- [24] H. Jiang, Y. Chen, X. Zheng, S. Jin, Q. Ma, A study on stable regularized moving least-squares interpolation and coupled with SPH method, *Math. Probl. Eng.* 2020 (2020) 9042615.
- [25] L. Hu, Q. HongFu, C. FuZhen, S. Chao, A particle refinement scheme with hybrid particle interacting technique for multi-resolution SPH, *Eng. Anal. Bound. Elem.* 118 (2020) 108–123.
- [26] T. Ye, D. Pan, C. Huang, M.B. Liu, Smoothed particle hydrodynamics (SPH) for complex fluid flows: recent developments in methodology and applications, *Phys. Fluids* 31 (2019).
- [27] H. Gotoh, A. Khayyer, On the state-of-the-art of particle methods for coastal and ocean engineering, *Coast. Eng. Jpn.* 60 (2018) 79–103.
- [28] A. Colagrossi, M. Landrini, Numerical simulation of interfacial flows by smoothed particle hydrodynamics, *J. Comput. Phys.* 191 (2003) 448–475.
- [29] I. Hammami, S. Marrone, A. Colagrossi, G. Oger, D. Le Touzé, Detailed study on the extension of the δ -SPH model to multi-phase flow, *Comput. Methods Appl. Mech. Eng.* 368 (2020) 113189.
- [30] N. Grenier, M. Antuono, A. Colagrossi, D. Le Touzé, B. Alessandrini, An Hamiltonian interface SPH formulation for multi-fluid and free surface flows, *J. Comput. Phys.* 228 (2009) 8380–8393.
- [31] S. Adami, X.Y. Hu, N.A. Adams, A new surface-tension formulation for multi-phase SPH using a reproducing divergence approximation, *J. Comput. Phys.* 229 (2010) 5011–5021.
- [32] A.M. Tartakovsky, A. Panchenko, Pairwise force smoothed particle hydrodynamics model for multiphase flow: surface tension and contact line dynamics, *J. Comput. Phys.* 305 (2016) 1119–1146.
- [33] X.Y. Hu, N.A. Adams, A multi-phase SPH method for macroscopic and mesoscopic flows, *J. Comput. Phys.* 213 (2006) 844–861.
- [34] Z. Chen, Z. Zong, M.B. Liu, L. Zou, H.T. Li, C. Shu, An SPH model for multiphase flows with complex interfaces and large density differences, *J. Comput. Phys.* 283 (2015) 169–188.
- [35] M. Rezavand, M. Taeibi-Rahni, W. Rauch, An ISPH scheme for numerical simulation of multiphase flows with complex interfaces and high density ratios, *Comput. Math. Appl.* 75 (2018) 2658–2677.
- [36] A. Khayyer, H. Gotoh, Y. Shimizu, A projection-based particle method with optimized particle shifting for multiphase flows with large density ratios and discontinuous density fields, *Comput. Fluids* 179 (2019) 356–371.
- [37] X.Y. Hu, N.A. Adams, An incompressible multi-phase SPH method, *J. Comput. Phys.* 227 (2007) 264–278.
- [38] X.Y. Hu, N.A. Adams, A constant-density approach for incompressible multi-phase SPH, *J. Comput. Phys.* 228 (2009) 2082–2091.
- [39] S. Shao, Incompressible smoothed particle hydrodynamics simulation of multifluid flows, *Int. J. Numer. Methods Fluids* 69 (2012) 1715–1735.
- [40] S.J. Lind, P.K. Stansby, B.D. Rogers, Incompressible–compressible flows with a transient discontinuous interface using smoothed particle hydrodynamics (SPH), *J. Comput. Phys.* 309 (2016) 129–147.
- [41] P. Nair, G. Tomar, Simulations of gas-liquid compressible-incompressible systems using SPH, *Comput. Fluids* 179 (2019) 301–308.
- [42] Q. Yang, J. Yao, Z. Huang, M. Asif, A comprehensive SPH model for three-dimensional multiphase interface simulation, *Comput. Fluids* 187 (2019) 98–106.
- [43] P.N. Sun, D. Le Touzé, G. Oger, A.M. Zhang, An accurate SPH volume adaptive scheme for modeling strongly-compressible multiphase flows. Part 1: numerical scheme and validations with basic 1D and 2D benchmarks, *J. Comput. Phys.* 426 (2021) 109937.
- [44] M. Rezavand, C. Zhang, X.Y. Hu, A weakly compressible SPH method for violent multi-phase flows with high density ratio, *J. Comput. Phys.* 402 (2020).
- [45] Z.F. Meng, P.P. Wang, A.M. Zhang, F.R. Ming, P.N. Sun, A multiphase SPH model based on Roe's approximate Riemann solver for hydraulic flows with complex interface, *Comput. Methods Appl. Mech. Eng.* 365 (2020).
- [46] Q. Yang, F. Xu, Y. Yang, J. Wang, Two-phase SPH model based on an improved Riemann solver for water entry problems, *Ocean Eng.* 199 (2020) 107039.
- [47] P. Suresh, S.S.P. Kumar, B.S.V. Pantaik, A comparative study of two different density estimation techniques for multi-phase flow simulations using SPH, *Int. J. Comput. Methods Eng. Sci. Mech.* 20 (2019) 29–47.
- [48] M. Antuono, A. Colagrossi, S. Marrone, C. Lugni, Propagation of gravity waves through an SPH scheme with numerical diffusive terms, *Comput. Phys. Commun.* 182 (2011) 866–877.

- [49] P. Sun, A. Colagrossi, S. Marrone, A. Zhang, The δ -plus-SPH model: simple procedures for a further improvement of the SPH scheme, *Comput. Methods Appl. Mech. Eng.* 315 (2016).
- [50] D.H. Zhang, Y.X. Shi, C. Huang, Y.L. Si, B. Huang, W. Li, SPH method with applications of oscillating wave surge converter, *Ocean Eng.* 152 (2018) 273–285.
- [51] X. Zheng, Q. Ma, S. Shao, Study on SPH viscosity term formulations, *Appl. Sci. (Switzerland)* 8 (2018).
- [52] D.D. Meringolo, A. Colagrossi, S. Marrone, F. Aristodemo, On the filtering of acoustic components in weakly-compressible SPH simulations, *J. Fluids Struct.* 70 (2017) 1–23.
- [53] F. He, H.S. Zhang, C. Huang, M.B. Liu, Numerical investigation of the solitary wave breaking over a slope by using the finite particle method, *Coast. Eng.* 156 (2020) 103617.
- [54] A. Colagrossi, E. Rossi, S. Marrone, D. Le Touzé, Particle methods for viscous flows: analogies and differences between the SPH and DVH methods, *Commun. Comput. Phys.* 20 (2016) 660–688.
- [55] M. Antuono, A. Colagrossi, The damping of viscous gravity waves, *Wave Motion* 50 (2013) 197–209.
- [56] M.D. Green, J. Peiró, Long duration SPH simulations of sloshing in tanks with a low fill ratio and high stretching, *Comput. Fluids* 174 (2018) 179–199.
- [57] T. Hu, S. Wang, G. Zhang, Z. Sun, B. Zhou, Numerical simulations of sloshing flows with an elastic baffle using a SPH-SPIM coupled method, *Appl. Ocean Res.* 93 (2019) 101950.
- [58] J.R. Shao, H.Q. Li, G.R. Liu, M.B. Liu, An improved SPH method for modeling liquid sloshing dynamics, *Comput. Struct.* 100–101 (2012) 18–26.
- [59] X.Y. Cao, F.R. Ming, A.M. Zhang, Sloshing in a rectangular tank based on SPH simulation, *Appl. Ocean Res.* 47 (2014) 241–254.
- [60] A. Rafiee, F. Pistani, K. Thiagarajan, Study of liquid sloshing: numerical and experimental approach, *Comput. Mech.* 47 (2011) 65–75.
- [61] C. Huang, T. Long, S.M. Li, M.B. Liu, A kernel gradient-free SPH method with iterative particle shifting technology for modeling low-Reynolds flows around airfoils, *Eng. Anal. Bound. Elem.* 106 (2019) 571–587.
- [62] S. Adami, X.Y. Hu, N.A. Adams, A generalized wall boundary condition for smoothed particle hydrodynamics, *J. Comput. Phys.* 231 (2012) 7057–7075.
- [63] A. Mokos, B.D. Rogers, P.K. Stansby, J.M. Domínguez, Multi-phase SPH modelling of violent hydrodynamics on GPUs, *Comput. Phys. Commun.* 196 (2015) 304–316.
- [64] X.Y. Cao, F.R. Ming, A.M. Zhang, L. Tao, Multi-phase SPH modelling of air effect on the dynamic flooding of a damaged cabin, *Comput. Fluids* 163 (2018) 7–19.
- [65] L. Lobovský, E. Botia-Vera, F. Castellana, J. Mas-Soler, A. Souto-Iglesias, Experimental investigation of dynamic pressure loads during dam break, *J. Fluids Struct.* 48 (2014) 407–434.